

INVESTIGATIONS OF MAGNETIC/ELECTRIC FIELD CONTROL OF MAGNETI-
ZATION OF FERROMAGNETIC AND MULTIFERROICS

by

YUZAN XIONG

A dissertation submitted in partial fulfillment of the
requirements for the degree of

DOCTOR OF PHILOSOPHY IN ELECTRICAL ENGINEERING

2022

Oakland University
Rochester, Michigan

Doctoral Advisory Committee:

Hongwei Qu, Ph.D., Chair

Wei Zhang, Ph.D.

Jia Li, Ph.D.

Ankun Yang, Ph.D.

Meir Shillor, Ph.D.

© Copyright by Yuzan Xiong, 2022
All rights reserved

ACKNOWLEDGMENTS

First and foremost, I want to express my sincere gratitude to Prof. Hongwei Qu and Prof. Wei Zhang for the important guidance they gave me over the period of the last six years as I pursued my Ph.D. I wish to express my appreciation for their assistance in providing me with academic knowledge, research instructions, and professional career advice. I would also like to express my thanks to the rest of the professors on my Doctoral Advisory Committee (DAC) members: Dr. Ankun Yang, Dr. Jia Li, and Dr. Meir Shillor, for their constructive suggestions for my research.

When I was a visiting graduate student at Argonne National Laboratory (ANL), Dr. Yi Li, who was my labmate there, helped me with countless hours of technical support with material characterizations and micro-/nano-fabrications. Over the years, working with him has been a great pleasure and an experience I will never forget. I want to convey my sincere gratitude to Dr. Novasad Valentine for giving me this chance at ANL. Additionally, I would want to express my thankfulness to Dr. John Pearson for his kindness, assistance, and superior management.

I am also very appreciative of all the staff members at Center for Nanoscale Materials (CNM) for their careful maintenance of the workspace, instructions, and technical assistance with a variety of tools. I would especially like to thank Dr. Ralu Divan for all her assistance and conversations. Without their unwavering support and suggestions, I would not have developed into the person I am today.

Last but not least, without the support of the National Science Foundation (NSF), this research would not have been achievable. In particular, I want to express my sincere gratitude to my family members for their compassion, steadfast moral support, and encouragement in helping me manage my stress.

Yuzan Xiong

ABSTRACT

INVESTIGATIONS OF MAGNETIC AND ELECTRIC FIELD CONTROL OF MAGNETIZATION DYNAMICS OF FERROMAGNETIC AND MULTIFERROICS

by

YUZAN XIONG

Adviser: Hongwei Qu, Ph.D.

The shortcomings of contemporary complementary metal oxide semiconductor (CMOS) technologies include increased power consumption, scalability, volatility, and device variability. New materials and novel devices are being investigated in this regard. Spintronic devices, which are normally based on magnetic materials, store and process data based on the modes of electron spins, rather than the presence or absence of charges as in the CMOS, are one possible approach. Numerous potential advantages of spintronic devices include its quick operational speed, low power requirement, and non-volatility. Two ferromagnetic materials suitable for creating spintronic devices are investigated in this dissertation study. Material properties, techniques for regulating the magnetization of materials, with both magnetic and electrical fields, and the development of devices useful for use in frequency modulations are all respectively detailed.

The first section of this dissertation studies the magnetically-induced transparency (MIT) effect in $Y_3Fe_5O_{12}$ (YIG)/Permalloy (Py) coupled bilayers. The measurement is achieved via a heterodyne detection of the coupled magnetization dynamics using a

single wavelength that probes the magneto-optical Kerr and Faraday effects of Py and YIG, respectively. Clear features of the MIT effect are evident from the deeply modulated ferromagnetic resonance of Py due to the perpendicular-standing-spin-wave of YIG. We develop a phenomenological model that nicely represents the experimental results including the induced amplitude and phase evolution caused by the magnon-magnon coupling. This work offers a new route towards studying phase-resolved spin dynamics and hybrid magnonic systems.

The second part of this dissertation discusses the research on the hexaferrite material, Zn_2Y , and the prospect of controlling its magnetic characteristics by applying a dc voltage, which is akin to a bias electric field. The detection and investigation of the magnetoelectric (ME) effect for in-plane currents orthogonal to the hexagonal axis in single crystal and thin films of Zn_2Y grown via liquid phase epitaxy. By applying a dc voltage, tuning of ferromagnetic resonance (FMR) was achieved in the hexaferrites. In addition to the frequency shift caused by the electrical tuning, magnetic properties of the material as a function of the input tuning power was also studied.

TABLE OF CONTENTS

ACKNOWLEDGMENTS	iv
ABSTRACT	vi
LIST OF TABLES	x
LIST OF FIGURES	x
CHAPTER ONE	
INTRODUCTION	1
1.1 Motivation	1
1.2 Background and Overview	2
1.3 Outline of Dissertation	9
CHAPTER TWO	
THEORETICAL BACKGROUND	11
2.1 Magnetism	12
2.2 Magnetic Moment and Magnetization	15
2.3 Spintronics	18
2.3.1 GMR	20
2.3.2 Spin Transfer Torque (STT)	22
2.3.3 Magnetization Dynamics	25
2.4 Magneto-Optical Phenomena	30

TABLE OF CONTENTS—Continued

2.4.1 Magneto-Optical Faraday Effect (MOFE)	33
2.4.2 Magneto-Optical Kerr Effect (MOKE)	35
2.5 Coplanar Waveguide	38
CHAPTER THREE	
THIN FILM'S STRUCTURE, DEPOSITION, AND CHARACTERIZATIONS	42
3.1 Introduction to YIG Spintronics and Thin Film Growth and Characterization	43
3.1.1 Crystal Structure and Magnetic Properties	44
3.1.2 Deposition of Thin Films	47
3.1.3 Characterizations of the YIG Thin Film	52
3.2 Magnetoelectric and Multiferroics	62
CHAPTER FOUR	
PROBING MAGNON-MAGNON COUPLING IN EXCHANGED COUPLE YIG/PY BILAYERS WITH MAGNETO-OPTICAL EFFECTS	69
4.1 Experimental Setup	69
4.2 Results and Discussion	74
CHAPTER FIVE	
HEXAGONAL FERRITE-BASED BAND-PASS FILTER WITH DUAL MAGNETIC AND ELECTRIC FIELD TUNABILITY	86
5.1 Experimental Setup	88
5.2 Results and Discussion	91
CHAPTER SIX	
SUMMARY AND OUTLOOK	97
REFERENCES	99

LIST OF TABLES

Table I	Definition of MOKE geometries.	36
Table II	Key magnetic properties and corresponding methods of measurement.	53

LIST OF FIGURES

Figure 1	Magnets with similar poles pointing towards each other feel a repulsive force while magnets with opposite poles feel an attractive force.	13
Figure 2	A simple depiction of an electron orbiting the atomic nucleus. The spin (s) is depicted as the intrinsic spin of the electron.	14
Figure 3	A spinning electron with angular momentum, LS , results in a spin magnetic moment.	16
Figure 4	Illustration of a spin wave propagating. The arrows represents the direction of the magnetization through the lattice.	17
Figure 5	The magnetization of FM layer precesses around the external dc magnetic field direction under FMR.	18
Figure 6	The magnetic spin of an electron in the direction of magnetic field lines.	19
Figure 7	Schematic representation of the GMR effect.	21
Figure 8	Spin transfer torque in a ferromagnet/spacer/ferromagnet structure for electron flow directions favoring (a) parallel	23
Figure 9	Schematic of the precession of the magnetic moment μ_s around the external magnetic field H .	27
Figure 10	Schematic illustration of the Landau-Lifshitz-Gilbert equation.	30
Figure 11	The three bases for the two states of polarized light.	31
Figure 12	Linearly polarized light can be decomposed into two circular polarized components.	32

LIST OF FIGURES—Continued

Figure 13	The MOFE.	34
Figure 14	Schematic of the three different MOKE configurations: (a) Polar, (b) Longitudinal, and (c) Transverse MOKE geometries and the effect on arbitrarily polarized light incident at angle θ .	37
Figure 15	Illustration of the flip-chip orientation of a magnetic sample, shown in purple, placed face-down on a CPW, shown in gold.	38
Figure 16	Distributed circuit model of a CPW.	40
Figure 17	Crystalline structure of Yttrium Iron Garnet ($\text{Y}_3\text{Fe}_5\text{O}_{12}$) ^[145] .	46
Figure 18	A schematic diagram of a rf-sputtering system.	49
Figure 19	Pick-up coil geometry and theoretical response signal of ideal dipole versus scan length in a MPMS SQUID magnetometer.	54
Figure 20	Schematic of a Josephson junction.	55
Figure 21	The incident wave will be reflected and/or transmitted after entering the device under test (DUT).	57
Figure 22	Two-port device S-parameters model.	58
Figure 23	Block diagram of the VNA-FMR spectrometer built in this dissertation.	59
Figure 24	In-plane FMR, with the magnetization parallel to the thin film and the applied magnetic field.	61
Figure 25	Out-of-plane FMR, with the magnetization perpendicular to the film and the applied magnetic field.	61

LIST OF FIGURES—Continued

Figure 26	Schematic diagram for a multiferroic and magnetoelectric ordering in materials controlled by ferroelectric and ferromagnetic behaviors of the materials.	66
Figure 27	Configurations for propagation of FVMSW, BVMSW, and MSSW, respectively.	69
Figure 28	Schematic of the measurement setup.	71
Figure 29	Schematic illustration of the experimental setup.	72
Figure 30	Example signal trace for YIG/Py (solid) and YIG/SiO ₂ /Py (dashed) measured at 5.85 GHz.	74
Figure 31	(a) Lorentzian fits for the Re[Vo] dataset of the 10-nm-Py sample at the same frequency window.	75
Figure 32	Dataset for the 10-nm-Py sample.	76
Figure 33	Plotting and the fitting of the observed PSSW modes versus the resonance fields.	77
Figure 34	Theoretical signal trace of the MIT effect of the YIG/Py bilayer, 7 hybrid PSSW modes are shown as an example.	78
Figure 35	Dataset for the 30-nm-Py sample.	79
Figure 36	(a) Full scan of the signals, Vo , as a function of the magnetic field and frequency.	81
Figure 37	Fine-scans at smaller field and frequency steps corresponding to the boxes in Figure 36 (5.7 ~ 6.3 GHz).	81
Figure 38	Dataset for the reference samples.	82
Figure 39	The Re[Vo] signal at a representative frequency window (5.85 ~ 6.1 GHz) for the 10-nm-Py sample.	83
Figure 40	YIG PSSW lineshape (12 modes series near the Py resonance	

LIST OF FIGURES—Continued

	are labeled and analyzed, $n = 32 \sim 43$) after subtracting the Py resonance profile.	84
Figure 41	(a) Resonance field, HPSSWYIG of the PSSW series and the HFMRPy envelope.	85
Figure 42	Schematics of the ferrite-based band-pass filter prototype showing the position of Zn ₂ Y magnetostatic resonator atop of the short-circuited microstrip line and bias permanent magnet inside the filter's frame.	89
Figure 43	Schematics of the FMR measurement of the ferrite material, Zn ₂ Y, on top of a microstrip transmission line with a series of bias external magnetic fields.	90
Figure 44	Schematics of the small DC voltage applied to the ferrite material, Zn ₂ Y, which mounts on top of the transmission line.	91
Figure 45	The measured transmission characteristics (a) and reflection coefficient (b) of the bandpass filter under different bias fields.	92
Figure 46	Comparison between the measured filter's characteristics for the opposite directions of the signal propagation.	93
Figure 47	Band-pass filter performance throughout the X-band: (a) insertion loss, (b) 3-dB bandwidth.	94
Figure 48	(a) Characteristics tuning by applied DC current due to the nonlinear ME effect.	96

CHAPTER ONE

INTRODUCTION

The amount of research devoted to investigating and creating new computing paradigms as substitute technologies for traditional CMOS devices has significantly increased recently. Moore's law, which asserts that the number of transistors per chip would double roughly every 18 to 24 months, has been applied to CMOS for more than 40 years. Moore's law is expected to end and CMOS scaling to saturate, which has led to an upsurge in the development of beyond-CMOS devices in an effort to get around CMOS scaling's constraints.

1.1 Motivation

Early forecasts suggest that Moore's law would already have ended, yet CMOS has continued to scale. Upon first, it was thought that constraints like lithography restrictions or gate oxide thickness would be the limiting factors; however, processing and material research have helped to resolve these problems. While it was previously believed that feature sizes below the wavelength of the exposure tool were not feasible and would limit the size of the device, new patterning methods like pitch division, phase shift lithography, as well as the development of new exposure techniques like extreme ultraviolet exposure have made it possible to pattern even smaller devices. Furthermore, it was thought that when device sizes were shrunk, the gate oxide thickness would also need to

be reduced in size, leading to significant leakage current and finally gate oxide breakdown. Although scaling in CMOS does not seem to be coming to an end anytime soon, it is generally accepted that in order to solve scaling-related problems, beyond-CMOS devices must be developed. As devices get closer to the atomic scale, their physical dimensions will most likely be where scaling comes to an end. It will become harder and harder to make devices smaller as they already approach dimensions that are only a few atomic layers thick.

Device performance is also a problem because devices are scaled continuously. Device scaling has downsides such as an exponential increase in leakage current and increased device variability, while it increases capacitance and decreases voltage. Leakage current in more recent generations of devices has greatly increased and now a significant portion of the energy needed for operation is due to the thin gate oxides. Additionally, as devices are scaled, they become more sensitive to slight changes in processing, which can have a significant impact on how well they function. Beyond-CMOS devices are being explored to overcome the approaching end of Moore's law.

1.2 Background and Overview

The phenomena associated with the operation of micro- and nano-scale magnetic devices will be discussed. The first thorough investigation of the behavior of lodestones was conducted by P. Peregrinus, who reported his insights in a letter in 1269^[1]. His study is significant for the strong emphasis he places on testing as the foundation for his

conclusions. He demonstrated that magnets have north and south poles and unlike poles attract. His work may possibly have contributed to the discovery of magnetic field lines surrounding lodestones using small needles of irons. The understanding of magnetism grown dramatically in the 19th century. F. Bloch argued in 1930 that the shift in a material's saturation magnetization towards absolute zero may be explained by the occurrence of spin waves in magnetically ordered materials. By observing the ferromagnetic metals showed peak in their resistance when exposed to high-frequency radiation and applied magnetic fields, Griffiths made the first experimental observation of spin waves in 1946^[2].

Spin waves (SWs) are wave-like excitations in magnetic materials – the waves propagate by either exchange or dipole interactions between precessing spins. SWs can be understood as particular, wave-type solutions of the time-dependent Landau-Lifshitz-Gilbert equation (LLG). The LLG equation describes the dynamics of the $M(r, t)$ magnetization distribution. SWs can transmit spin information over macroscopic distances in the absence of Joule heating^[3-8]. To manipulate the propagation of SWs, various methods such as lithographically defined synthetic crystal^[9, 10], static magnetic fields^[11, 12], and electrical currents have been used^[13-16]. A major challenge for experimentally studying the SW transmission in the presence of domain walls is that resonant excitation and coherent propagation of SWs require well-defined quantization axes for spins. In existing studies, this condition is usually realized through the application of a large external magnetic field, which prevents the formation of more than one magnetic domain. A domain

wall in a ferromagnetic material is a boundary between differently magnetized regions, and its motion provides a convenient scheme to control the magnetization state of the material. Domain walls can be confined and moved along nanostrips of magnetic thin films, which are proposed platforms for next generations of solid-state magnetic memory-storage and logic devices.

Elementary particles carry spin, which is an intrinsic form of angular momentum. Spintronics is a relatively young field of study that has evolved in recent decades to examine the study of spin transport in magnetic materials^[17, 18]. Spintronics is based on the spin dependent density of states of the ferromagnetic materials^[19]. Ferromagnetic materials play a significant role in spin transport and magnetism due to the energy difference between spin up and spin down states^[20]. This results in different scattering environment for electrons at different spin states which results in a spin polarized current when an electrical current flows through a ferromagnetic material. The electronic density of states within a ferromagnetic material becomes spin dependent under a magnetic field which allows spin injection and detection throughout ferromagnetic materials^[17]. The development of electrical systems that make use of both the electrons' charge and spin is the focus of the field of spintronics^[17]. Even though N. Mott stressed the significance of the electron's spin in controlling transport properties in 1936 to understand the electrical conductivities of transition metals and their alloys^[21], the remarkable scientific and technological advancements in this field all began with the discovery of giant magnetoresistance (GMR) in metallic magnetic multilayers Fe/Cr by A. Fert and P. Grunberg in 1988^[22, 23]

and spin valves have been extensively studied to understand the spin properties of semiconductors and new channel materials^[24, 25].

GMR is definitely one of the most influential phenomena in the magnetoelectronics area. It is the change in magnetoresistance in an artificial multilayer structure that consisted from thin metallic non-ferromagnetic and ferromagnetic layers^[26]. A magnetic field is able to change the magnetization of adjacent ferromagnetic layers from antiparallel to parallel configuration. This property in thin film structures opened a wide variety of application for GMR sensors including magnetic field sensors and write/read heads for hard disk drives^[27]. In application involving sensing for disk drives, it has later been replaced by spin-dependent tunneling devices, in which the metal spacer is swapped out for an insulating barrier, and the magnetoresistance of the device increases at room temperature relative to the GMR counterpart by a factor of 10.

Magnetic tunnel junctions (MTJs) or tunneling magnetoresistance (TMR) devices are the terms used to describe these sensing heads. In 1975, Julliere measured the properties of Fe/Ge/Co junctions and observed TMR of 14% at low temperatures^[28]. However, his results were not able to be reproduced until 1982 by Maekawa and Gafvert, which showed 2% TMR in a Ni/NiO/Co junction at 4.2K^[29]. In the subsequent decade, many experiments were attempted to achieve higher TMR at room temperature. Most of these results have low TMR ratio $< 1\%$ at low temperatures, until Moodera *et al.*^[30] and Miyazaki *et al.*^[31] demonstrated large room temperature TMR $> 10\%$ with amorphous Al-O as spacer layer independently. In 1995, Miyazaki *et al* reported room temperature TMR up

to 18% in Fe/Al₂O₃/Fe junctions, and 30% at 4.2K. The Al-O layer was prepared by oxidation in air for 24 hours. Moodera also used Al-O as tunneling barriers but using oxygen plasma to oxidize aluminum. The CoFe/Al₂O₃/Co junctions had TMR ~ 10% and the results were reproducible. Crystalline MgO would have better characteristics, according to calculations by Butler *et al.*^[32] and Mathon *et al.*^[33], and as a result, room temperature TMR values reached as high as 600%^[34] and 1000%^[35].

Another important prediction and discovery in the development of spintronics is the so-called spin-transfer torque (STT) effect, which is first introduced by J.C. Slonczewski and L. Berger^[36-41], gives means to field-free electrically manipulate the magnetic moment of a ferromagnet. STT provides an interface between localized magnetic moments and magnetization currents, associated with the motion of quasi-particle with a finite magnetic moment. STT, for instance, couple the excitation of the magnetic moments in the insulating, magnetically ordered material to the spatial distribution of electron spins in an adjacent metallic layer. Even in nonmagnetic materials, this also affects the electric properties of the metal and can therefore be detected with relative ease.

From technological point of view, GMR's and later on TMR's application to the read heads of the hard disk drives (HDDs) has led to a solid increase of the areal recording density for many years^[42]. The magnetic random-access memory (MRAM)^[42-44] utilizes the MTJs as the memory cell to achieve nonvolatile memory operations with short access time. Advances in MRAM technology have been closely linked with advances in

the study of spintronics: the magnetic state is read through large TMR and usually written by STT method.

Additionally, magnetic excitations in magnetically ordered system, spin waves (SWs) or magnons^[3, 6, 45], are an ideal spin current carrier in spintronics. Magnons are quantized low-energy elementary excitations in ferromagnets. In addition to their energy and crystal momentum, magnons are known to have intrinsic angular momentum. Therefore, the translational flow of quasiparticle magnons can be identified as pure spin current since magnons are naturally chargeless.

The development of electronic technology is flexibly related to the progresses made in material science. Functional materials out of the broad class of materials available today offer unique chance for developing novel components and devices. Three well-known forms of ferroic orders are ferroelectricity, ferroelasticity, and ferromagnetism. Ferromagnetic and ferroelectric materials exhibit spontaneous magnetization and spontaneous electric polarization, respectively. Ferroelasticity manifests itself as a spontaneous strain, produced by a stress induced phase change. The multiferroics, combine two or more different ferroic orders in a single phase and are utilized in a broad range of systems. The strong coupling between both charge and spin orderings is essential for employing in the field of spintronics and other allied areas. These types of materials have electric polarization proportionate to external magnetic field and generate magnetization proportionate to the external electric field.

Magnetoelectric (ME) materials are of utmost interest in view of both fundamental understanding and novel desirable applications. An electric field can switch its ferromagnetic surface magnetization and thus control exchange bias-based spin valve devices. ME response has been realized in stress-strain coupled multiphase magnetoelectric composites like BaTiO₃/Fe and in PZT/FeBSiC.

Modern physics places a high value on precision, and the Faraday effect has recently developed into a precision measurement tool with numerous uses. For instance, it is employed in precision magnetometers to test fundamental symmetries[46], to measure spin-noise[47], to measure the permanent electric dipole moments in atoms[48], to ascertain the strengths and directions of magnetic fields in the intergalactic medium[49], to determine magnetic field strengths and direction in atoms, or to investigate the process of light squeezing[50]. However, because these applications require the interaction of the probing light with the electric charge, the examined systems' electric polarizabilities are what cause the rotations to occur. A similar effect should be present due to the magnetic interaction of light in addition to this electrically driven rotation. This magnetic Faraday effect would provide new insights into the fundamental characteristics of magnetic materials.

Additionally, researchers frequently measure the ferromagnetic resonance (FMR) based on a vector network analyzer (VNA) and a coplanar waveguide (CPW) in order to explore the properties of magnetic films and nanostructures^[51-54]. The substrate is positioned to be the farthest away from the CPW, and a magnetic material sample is

positioned adjacent to the CPW's signal line. The precession of the magnetization is excited by a microwave magnetic field hrf proportionate to the rf current applied to the signal line of the CPW, which in turn causes a microwave voltage in the CPW. the approach is known as VNA-FMR^[53] or broadband-FMR^[55]. The FMR responses are retrieved from the scattering parameters (reflection coefficient (S_{11}) or transmission coefficient (S_{21})) measured by VNA. In general, only the changes in S_{21} or S_{11} due to the FMR absorption are of interest, and they are detected either in the frequency-swept mode^[52] or in the field-swept mode^[54]. The FMR absorption is measured at different frequencies in order to determine the effective saturation magnetization $4\pi M_{eff}$ and the damping constant α .

This dissertation covers the experimental measurement setup and characterization methods and techniques. Additionally, it also introduces basic concepts of spintronics and phenomena.

1.3 Outline of Dissertation

My research on the development of spintronics devices, that goes beyond CMOS, will be presented in this dissertation. The work will focus on my initiatives to develop fresh approaches to controlling the magnetization dynamics of materials as well as a novel detecting method for magnon-magnon coupling in exchange coupled bilayers (YIG/Py) with magneto-optical effects.

Chapter 2 will give the reader the background information on spintronic related phenomena and theory needed to understand the dissertation covered. The magnetization

dynamic, the GMR, and the STT effect will all be covered in the first three sections. The associated magneto-optical effects of the detection method will then be introduced. The ME effect of specifically multiferroic materials is introduced after that. The background of the CPW will be introduced in the last section of Chapter 2. The dynamic magnetic properties, deposition techniques, and feature of YIG thin films will be covered in Chapter 3. The experimental setup, methods, and materials utilized to investigate the magnon-magnon exchanged coupling between the YIG and Py thin films will be covered in Chapter 4. A novel method of controlling the magnetic properties of multiferroic materials by an electric field will be introduced in Chapter 5. Chapter 6 provides an overview of my research as well as current research initiatives pertaining to these subjects and suggested next study directions.

CHAPTER TWO

THEORETICAL BACKGROUND

The advancement of the integrated circuits (ICs) industries has been dominated for decades by complementary metal oxide semiconductor (CMOS) technology, which defines the generation, storage, transmission, and processing of information. However, with the current technology node shrunken to around 5-nm, CMOS has reached its physical limit and is now facing significant issues with area, power, and performance. With the data-intensive workloads as big data analytics, artificial intelligence, and bioinformatics require the hardware has greater performance for data storing and processing. The needs for beyond-CMOS technology is essential for producing electronics that are faster and more powerful. With CMOS downscaling, the need of viable alternatives for reducing the leakage of power increases and spin-based devices, due to its excellent features like non-volatility, low power consumption, and high read/write speed, appears as one of the most promising approaches to deal with this issue. Spin is an intrinsic form of angular momentum carried by elementary particles. In the past decades, the study of spin transport in magnetic materials has emerged as a relatively new research area known as spintronics^[17, 18, 56].

Spintronics is one of the emerging disciplines that continues to revolutionize the thriving field of information technology. The commercial impact of spintronics to data has been in the area of spin valves used in magnetic hard disk drives. The principle of

operation of such spin valves is based on the GMR effect. In order to fully understand the analysis in this dissertation, it is necessary to have some fundamental knowledge on the field of magnetism, spintronics, magneto-optical effects, and waveguides.

This chapter will give an introduction into the background of some of necessary components, phenomena, and applications. The relative orientation of the magnetization of two magnetic layers with a non-magnetic spacer layer can influence the electric current flow through the layers, which is referred to as magnetoresistance. The GMR in metallic structures will be introduced. Then the inverse phenomenon, the so-called STT, in which a current flow influences the magnetization direction by a transfer of angular momentum, is explained in a simple physical picture. The equation that describes the motion of the magnetization in a magnetic field, the Landau-Lifshitz-Gilbert (LLG) is introduced. Later on, magneto-optical effects, which is the principle for the unique detection method for the magnon-magnon coupling in YIG/Py bilayers, will be explained respectively. The CPW's fundamental ideas will next be introduced, along with design considerations.

2.1 Magnetism

A magnet is a magnetic dipole with two poles – north and south – where the opposite poles attract one another, and the similar poles repel each other. This is the fundamental knowledge of magnets. The Bohr-van Leeuwen theorem states that since the formation of magnetization in a solid cannot be fully described by a conventional

understanding of statistical or mechanical physics, and therefore, it is a quantum mechanical effect.

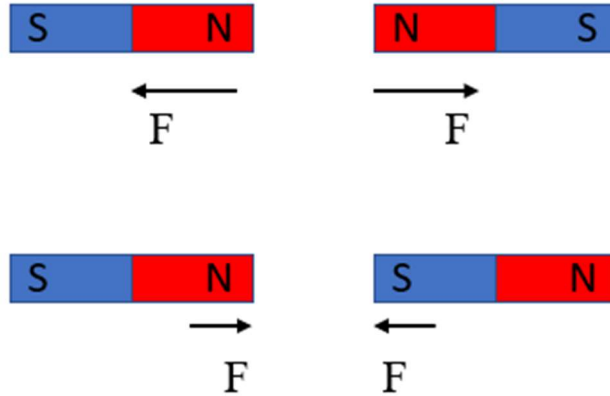


Figure 1. Magnets with similar poles pointing towards each other feel a repulsive force while magnets with opposite poles feel an attractive force.

Traditionally, it has been thought that a solid’s magnetization is made up of countless infinitesimally small loops of charge currents that are all rotating in the same direction. a magnetic dipole moment m is produced by these current loops:

$$|m| = \mu_0 IA \tag{1}$$

where I is the current and A is the area enclosed by the loop.

The Maxwell equations are then used to describe the relationship between the generated magnetic field and electric current as well as the relationship with the electric field^[57]. The idea of an electron’s spin (S) and orbital (l) quantum numbers was therefore proposed. In a straightforward atomic model, the spin S , can be thought of as the intrinsic angular momentum of the electron, while the orbital, denoted by the letter l , can be thought of as the angular momentum of the electron orbiting the nucleus.

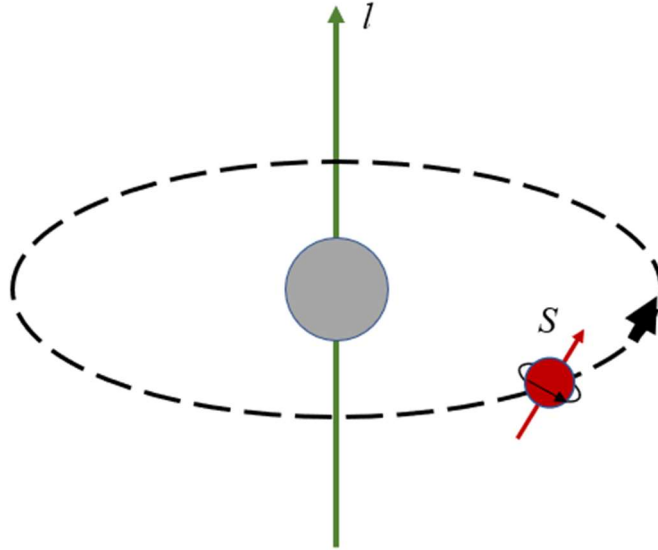


Figure 2. A simple depiction of an electron orbiting the atomic nucleus. The spin (s) is depicted as the intrinsic spin of the electron. The orbital angular momentum l is depicted as the orbital motion of the electron around the atomic nucleus. The spin of the nucleus is ignored in this picture.

The total magnetic moment of an atom can effectively be seen as:

$$m = -\frac{\mu_B}{\hbar} (g_s s + g_l l) \quad (2)$$

where μ_B is the Bohr magneton, \hbar is the reduced Planck constant and g_s (~ 2) and g_l ($= 1$) are the spin and orbital gyromagnetic ratios, respectively.

Magnetism of materials arises from the quantized magnetic moments – or “spins” – of electrons. Spins in most materials orient in random directions in the absence of an external magnetic field. However, spins in some materials align in the same direction even without an external magnetic field.

2.2 Magnetic Moment and Magnetization

As we all know, the matter is composed of atoms, and atoms are composed of atomic nuclei and electrons. In atoms, electrons have an orbital magnetic moment due to their movement around the nucleus. electrons have spin and the magnetic moments of atoms mainly come from the electronic magnetic moments, which are the source of all material magnetism.

The core component of magnetization is the magnetic moment, μ_m . A magnetic material is composed of atoms, each of which has a magnetic moment, μ_{mspin} , principally produced by the spin of the electron. A single electron's magnetic moment is a representation of its angular momentum. In magnetic materials, the electron's inherent spin angular momentum, L_s , is predominantly. The two possible spin states quantized by the reduced Planck's constant, \hbar . The spin gyromagnetic ratio is the ratio of the spin magnetic moment to the spin angular momentum.

$$\frac{\mu_{mspin}}{L_s} = \gamma_s \approx 1.76 \times 10^{11} \left(\frac{rad}{s \cdot T} \right) \approx 28 \left(\frac{GHz}{T} \right) \quad (3)$$

where μ_{mspin} is equal to $\pm\hbar e/2m_e$ which is frequently used and labeled as the Bohr magneton, μ_B ^[58].

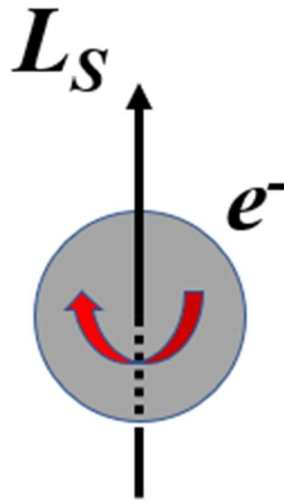


Figure 3. A spinning electron with angular momentum, L_S , results in a spin magnetic moment μ_{mspin} .

The magnetization of a sample is directly proportional to its magnetic moment, $M = m/V$, it reveals that the magnetization of a sample is directly proportional to its angular momentum.

Magnons are the quanta of spin waves, and carry a fixed amount of energy, lattice momentum, and spin in magnetic materials. They behave as weakly interacting quasiparticles obeying Bose-Einstein statistics. The use of magnons allows the implementation of novel wave-based computing technologies free from the drawbacks inherent to modern electronics, such as dissipation of energy due to Ohmic losses. A disturbance in local magnetic ordering can propagate in a magnetic material in the form of a wave, was predicted by F. Bloch in 1929^[45] and was named as spin wave as it is related to the collective excitations of the electron spin system in ferromagnetic metals and insulators.

Spin waves are generally excited in thin films and conduits fabricated in the form of narrow strips of a magnetic material. The most commonly used materials are polycrystalline metallic films of permalloy (Py, $\text{Ni}_{81}\text{Fe}_{19}$)^[3, 5] which combine a relatively low magnetic damping with good suitability for micro-sized patterning; and single crystal films of YIG which possess extremely low damping^[59, 60].

The classical approach for magnon excitation is the microwave technique, where an electromagnetic signal applied to a microwave antenna excites magnetization precession in the magnetic material via an alternating Oersted field induced around the antenna^[16, 61-63]. STT-based magnon injection will be discussed later in more detail as it enables the direct coupling of spin waves with a spin-polarized d.c. electric current and, thus, bridges magnonics with electron-based spintronics and electronics.

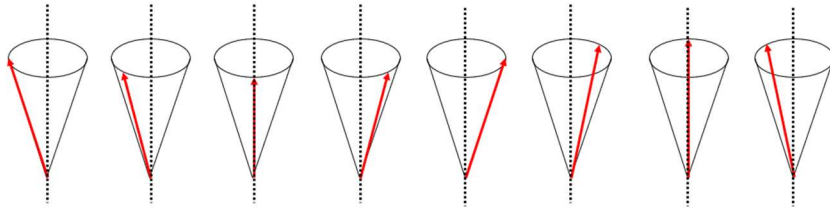


Figure 4. Illustration of a spin wave propagating. The arrows represent the direction of the magnetization through the lattice.

The concept of spin-waves represents a phase-coherent precession of magnetic moments or spins of a magnetically ordered system, as illustrated in *Figure 4*. Compared to one single spin flip, the energy of this spin-excited wavelike state has a much lower energy.

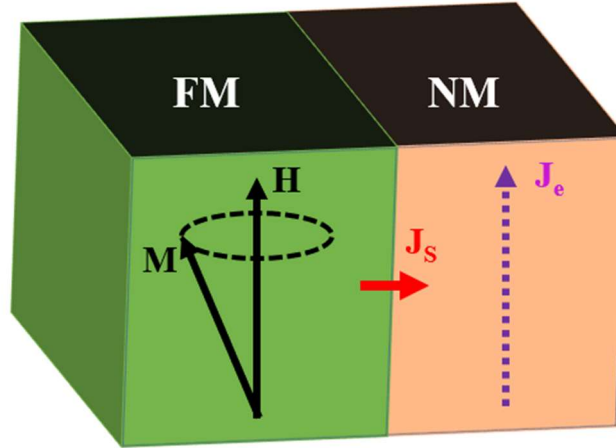


Figure 5. The magnetization of FM layer precesses around the external dc magnetic field direction under FMR. When the FM in resonance is in contact with a NM, the magnetization precession can pump a spin current J_S into adjacent NM layer. A charge current J_e is generated in NM via inverse spin hall effect (ISHE).

The name SWs are usually used to describe the phase-coherent, long wavelength excitations of the magnetic material. The ferromagnetic resonance (FMR) technique is a powerful way to excite SW with wavevector $q = 0$. For example, the spin pumping refers to the observation that the FM under FMR condition can effectively pump spin current into the adjacent non-magnetic layer, as illustrated in *Figure 5*.

2.3 Spintronics

According to Moore's law, the number of transistor on a chip doubles every year in the electronic industry. However, owing to the loss of chip stability, further downsizing is not possible below the critical dimension. Researchers now have another option to create microscopic devices based on modifying the spin degree of freedom thanks to the

development of spintronics. Spin electronics (or Spintronics) is the study of the intrinsic spin of the electron instead of or in addition to the charge of electrons in solid-state physics and has attracted much attention during the last decades because of its potential applications both in information storage and post complementary CMOS devices[42, 64].

An electron has two different intrinsic properties. One of them is the electronic charge property while the second one is the intrinsic spin of the electrons^[65](*Figure 6*).

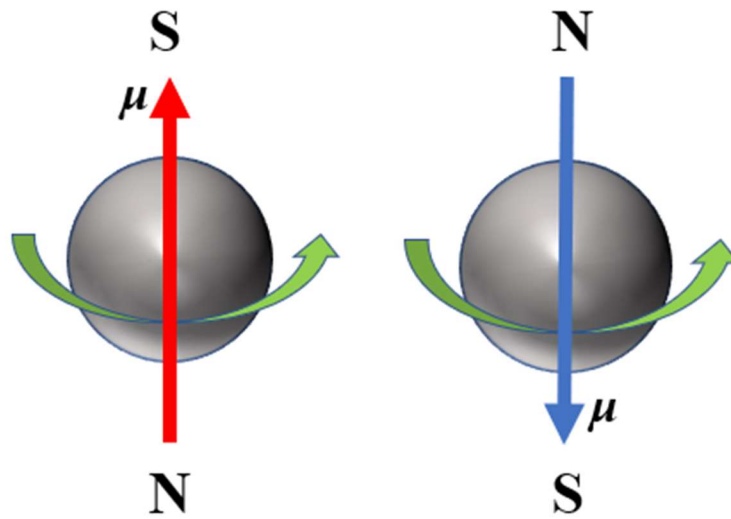


Figure 6. The magnetic spin of an electron in the direction of magnetic field lines

The active manipulation of an electron's degree of freedom for the purpose of storing information and detecting its associated magnetic moment in a solid-state device is the central focus of this multidisciplinary field^[66]. Recognizing the connection between a particle's spin and its solid-state surroundings is the goal of spintronics, which aims to apply this knowledge to create functional devices. In comparison to traditional

semiconductor devices, spin-based devices are known to process data more quickly, use less power, and have higher integration densities^[17, 18, 42, 66, 67]. Technologies already in use, like giant magnetoresistance-based memory devices^[27].

The angular momentum that an electron naturally possesses is known as spin. The magnetic field is produced by the motion of the spin, which also produces magnetic moment. In accordance with the spin axis, these spins function as a tiny bar magnet. Depending on how the electrons are spinning, like a top spinning anticlockwise (up) or clockwise (down) (see *Figure 6*). Spin is orientated arbitrarily and has no impact on current flow in a typical electric device. Spintronics devices create spin-polarized current and use the spin to control current flow. Spin polarization relates the difference between the number of spin-up and spin-down electrons participating in a certain electronics process. Spin-up (\uparrow) electrons means electrons with spin parallel to the magnetization, and spin-down (\downarrow) electrons are those antiparallel to the magnetization.

In the current age of the interest, we accumulate more and more data that needs to be stored. This growth of data demands faster and more efficient data storage technologies as currently, data centers worldwide already consume around 10% of the world's electricity production^[68-70].

2.3.1 GMR

GMR is the change of electric resistance of special structures when an external magnetic field is applied. It is a quantum mechanical effect which is based on spin-

dependent scattering phenomena in magnetic multilayers. The change in resistance of the multilayer occurs when the applied magnetic field aligns the magnetic moments of successive ferromagnetic layers (*Figure 7*). In the absence of applied magnetic field, the magnetic moments of magnetic layers are not aligned with respect to each other i.e., their magnetizations are antiparallel to each other, and it results in high resistance. By applying magnetic field, the magnetic moment of successive ferromagnetic layers gets aligned i.e., their magnetizations are parallel to each other, and it results in a drop in resistance of the multilayer.

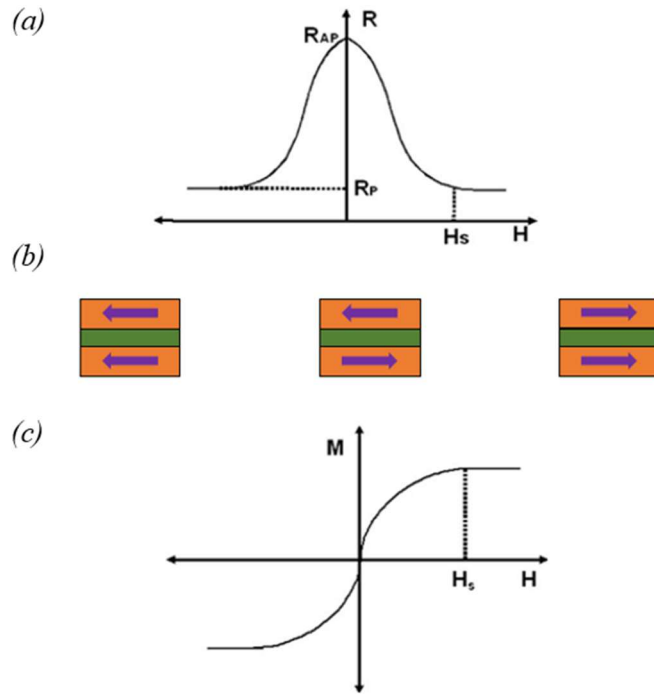


Figure 7. Schematic representation of the GMR effect. (a) Change in the resistance of the magnetic multilayer as a function of applied magnetic field. (b) The magnetization arrangement (indicated by the arrows) of the trilayer at various magnetic fields; the magnetizations are aligned antiparallel (AP) at zero field and are aligned parallel (P) when the external magnetic field $H >$ saturation field H_s . (c) M-H curve of the multilayer^[71].

The discovery of the GMR, independently discovered by A. Fert's group^[22] and P. Grunberg^[23] in late 1980s in Fe/Cr super lattice and Fe/Cr/Fe films, respectively, that is considered as the first big development in modern spintronics^[72] and recognized with the 2007 Nobel Prize in Physics. GMR is the abrupt change in resistance in magnetic multilayer structures when an external magnetic field is applied^[22, 23]. The resistance of the multilayer is at its minimum (maximum) when the spins in the ferromagnetic layers are aligned parallel (anti-parallel)^[22, 23]. The change in resistance due to changes in magnetization orientation is called magnetoresistance ratio and mathematically, GMR can be defined as:

$$GMR = \frac{R_{AP} - R_P}{R_P} \quad (4)$$

where R_P and R_{AP} are the resistances in parallel and antiparallel states.

The discovery of GMR opened the door to a new field – spintronics, which exploits the spin degrees of freedom of electrons along with its charge degree of freedom and it is at the helm of emerging nanotechnology. One of the most aspects of GMR discovery was that it was immediately turned into commercially available products – the first GMR hard disk head was introduced by IBM in 1997.

2.3.2 Spin Transfer Torque (STT)

The interaction between the spin and charge of electrons in magnetic multilayers becomes significant when scaled down to the nanoscale. Slonczewski^[36] and Berger^[73] made a theoretical prediction about an effect known as STT in 1996, which can be

defined as a spin-polarized current passing through a ferromagnetic layer will exert a torque on its magnetization (as shown in *Figure 8*). Local magnetization excitations like spin wave generation^[37, 38, 74], magnetic reversal or switching^[75], and stable precession^[76-78] can be caused by the STT. Instead of using the conventional Oersted field switching technique, the STT effect offers an electrical way to change the layer magnetization direction in a magnetic-based device.

Myers *et al.*^[79] reported the first experimental observation of STT-induced magnetization switching of the magnetization for a Co/Cu/Co point contact geometry in 1999, and Katine *et al.*^[75] observed the same phenomenon for a Co/Cu/Co nanopillar in 2000. Kiselev *et al.*^[77] reported the first STT-induced magnetization dynamics in Co/Cu/Co nanopillars shortly after in 2003.

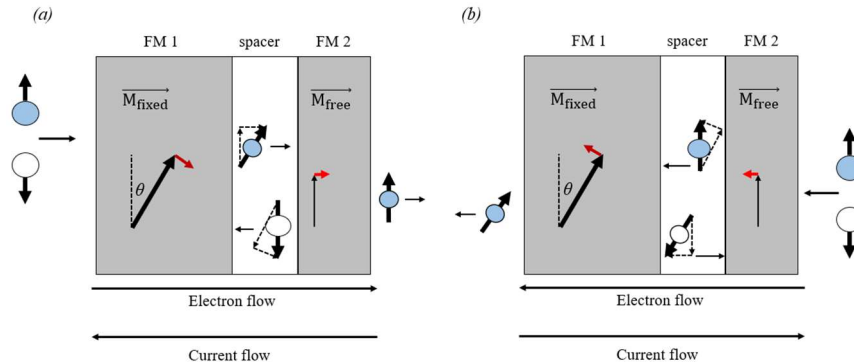


Figure 8. Spin transfer torque in a ferromagnet/spacer/ferromagnet structure for electron flow directions favoring (a) parallel and (b) antiparallel alignment. Due to a larger coercivity, the magnetization of FM 1 does not rotate due to the STT, whereas the magnetization of FM 2 follows the STT.

The electron flow from the fixed to the free layer and the two FM 1 and FM 2 magnetization directions, which are inclined by an angle of θ , are two examples to consider (*Figure 8 (a)*). According to the quantization axis of the magnetization, the wave function of the incident electrons is a superposition of spin-up and spin-down components. Due to the first ferromagnet's spin-dependent conductivity, after the electrons have traveled through FM 1, their magnetic moments will be polarized in the same direction as FM 1's magnetization.

Three distinct processes – spin filtering, differential spin reflection, and spatial spin precession – all result in the transverse angular momentum loss of the electrons as they move into the second ferromagnetic layer^[41, 80]. The second ferromagnetic layer, FM 2, detects the angular momentum since it must be conserved, and it exerts a torque on the magnetization. In comparison to the incident wave function, the reflected and transmitted wave functions for an electron are modified linear mixtures of majority and minority components. It was shown that the spin-dependent reflection and transmission causes a discontinuity in the transverse spin current, leading to a spin-transfer torque^[80].

The fixed layer spin polarizes electrons as they move from the fixed layer to the free layer through a magnetic tunnel junction (MTJ). The majority of the spins are aligned with the magnetization of the fixed layer. The spin angular momentum of these electrons would be transferred to the magnetic moment of the free layer as they approached it, until the magnetization of the free layer is parallel to the fixed layer. The magnetization of the free layer of the MTJ is forced to be antiparallel to the fixed layer if

the current direction is reversed and electrons are injected from the free layer of the MTJ. This allows us to switch the MTJ from a parallel (P) state to an antiparallel (AP) state, or vice versa by injecting a positive or negative current through it.

For the past 50 years, the only way to switch or excite magnetic moments was by using magnetic fields, but STT effect is an efficient method for magnon excitation by a charge current.

2.3.3 Magnetization Dynamics

In the following sections, I aim to introduce the fundamentals of magnetization dynamics, which is the common ground for the work that forms the basis of this dissertation.

The energy of a single electron spin in a static magnetic field H , is given by the Zeeman energy as:

$$E_S = -\mu_S \cdot H \quad (5)$$

where μ_S is the magnetic moment of the electron spin. From energy minimization, this results in the spin aligning with the magnetic field. The magnetic moment of the electron is related to the spin angular momentum S :

$$\mu_S = -\gamma_S S \quad (6)$$

where γ_S is the gyromagnetic ratio given by $\gamma_S = g_s e / 2m_e$. Here, e is the electron charge, g_s is the electron spin g-factor and m_e is the electron mass. However, the static magnetic field also exerts a torque τ on this magnetic moment, which is given by:

$$\tau = \mu_S \times H \quad (7)$$

As the torque is equal to the rate of change of angular momentum, one can combine Eqs. (6) and (7) to obtain:

$$\frac{d\mu_S}{dt} = -\gamma_S \mu_S \times H \quad (8)$$

From Eq. (8), one notices that rather than aligning the magnetic moment along the direction of the applied field, the torque causes a precession motion around H , as illustrated in . By solving Eq. (8), one can obtain the precession frequency ω_L , named the Larmor frequency:

$$\omega_L = \gamma_S H \quad (9)$$

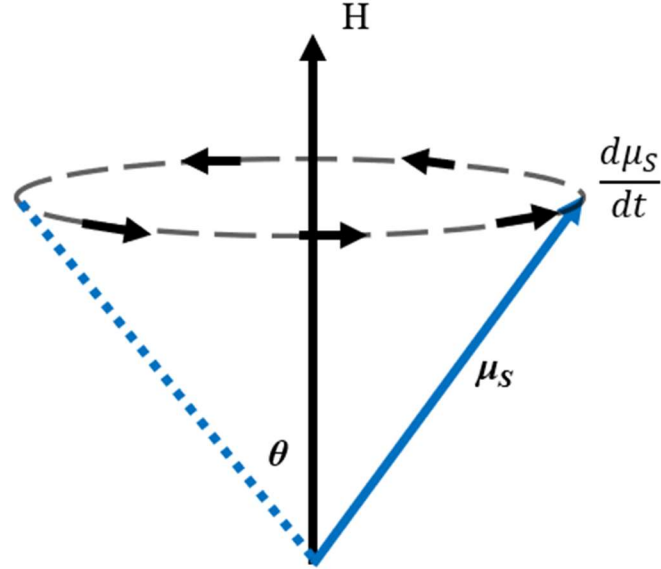


Figure 9. Schematic of the precession of the magnetic moment μ_S around the external magnetic field H . The precession angle θ is here severely exaggerated for illustration purposes.

Larmor precession is the governing principle behind FMR, which is important for the work performed in this dissertation, and it will be introduced in section 3.1.3.2.

The precessional motion of magnetic moments under the influence of an effective magnetic field is the base of magnetization dynamics. The precessional motion can be described by Landau-Lifshitz-equation, which was proposed by L. Landau and E. Lifshitz in 1935^[81]. Later on, Gilbert modified the equation by adding a magnetic damping term to it^[82]. The relation between the magnetic moment μ and the total angular momentum J can be expressed as $\mu = \gamma J$, where $\gamma = g\mu_B/\hbar$ is the gyromagnetic ratio, g is the g -factor of the electron ($g \approx 2.0023$), μ_B is the *Bohr* magnetron and $\hbar = h/(2\pi)$ is the Planck constant. A magnetic moment placed in an effective magnetic field B_{eff} experiences a torque:

$$\boldsymbol{\tau} = \boldsymbol{\mu} \times \mathbf{B}_{eff} \quad (10)$$

As $\tau = dJ/dt$, so the equation of motion for J can be written as

$$\frac{d\mathbf{J}}{dt} = \boldsymbol{\mu} \times \mathbf{B}_{eff} \quad (11)$$

where $B_{eff} = \mu_0 H_{eff}$. Here, the effective magnetic field H_{eff} is the sum of external and internal magnetic fields. It includes the externally applied static field H_0 , the dynamic component of externally applied magnetic field $H_M(t)$, the field generated due to the exchange interactions H_{ex} , the demagnetizing field H_d and the fields due to the shape and crystalline anisotropies H_{ani} .

$$\mathbf{H}_{eff} = \mathbf{H}_0 + \mathbf{H}_M(t) + \mathbf{H}_{ex} + \mathbf{H}_d + \mathbf{H}_{ani} + \dots \quad (12)$$

Now the atomic magnetic moment can be replaced by the macroscopic magnetization M . The effective field exerts a torque on the magnetization, corresponding to rate change of angular momentum due to which the magnetization starts to precess at Larmor frequency, $\omega = \gamma\mu_0 H_{eff}$. This precession of magnetization is described by the equation of motion called Landau-Lifshitz equation:

$$\frac{d\mathbf{M}}{dt} = -\gamma\mu_0 \mathbf{M} \times \mathbf{H}_{eff} \quad (13)$$

The system is non-dissipative, and the magnetization would precess around the static field indefinitely without reaching the equilibrium position with lower energy configurations with M parallel to H , and this contradicts reality. So, in 1935, Landau and Lifshitz formulated the equation of motion by introducing damping term^[81]:

$$\frac{d\mathbf{M}}{dt} = -\gamma\mu_0\mathbf{M} \times \mathbf{H}_{eff} - \frac{\lambda}{M_s} [\mathbf{M} \times (\mathbf{M} \times \mu_0\mathbf{H}_{eff})] \quad (14)$$

where λ is the damping constant. $\lambda = 1/\tau$ corresponds to the inverse relaxation time τ .

In 1955, Gilbert phenomenologically introduced a viscous damping term leading to the formulation of Landau-Lifshitz-Gilbert (LLG) equation:

$$\frac{d\mathbf{M}}{dt} = -\gamma\mu_0\mathbf{M} \times \mathbf{H}_{eff} + \frac{\alpha}{M_s} \left(\mathbf{M} \times \frac{d\mathbf{M}}{dt} \right) \quad (15)$$

where α is the dimensionless Gilbert damping parameter. This Gilbert damping parameter is viscous in nature, so with increase in the rotation of magnetization $d\mathbf{M}/dt$, the damping of the system increases. The LLG equation consists of two terms: precessional and damping term. The magnetization precesses along the applied field due to the torque proportional to $(\mathbf{M} \times \mathbf{H}_{eff})$ and the damping term is responsible for the relaxation of magnetization towards the equilibrium state. Due to this damping term, the magnetization follows a helical trajectory as shown below. It shows a realistic and damping precessional motion of the magnetization around the effective magnetic field. So we can say that the damping torque provides a dissipative mechanism through which energy and the spin angular momentum (magnon system) is transferred to the phonons in the lattice via spin-orbit interaction^[83].

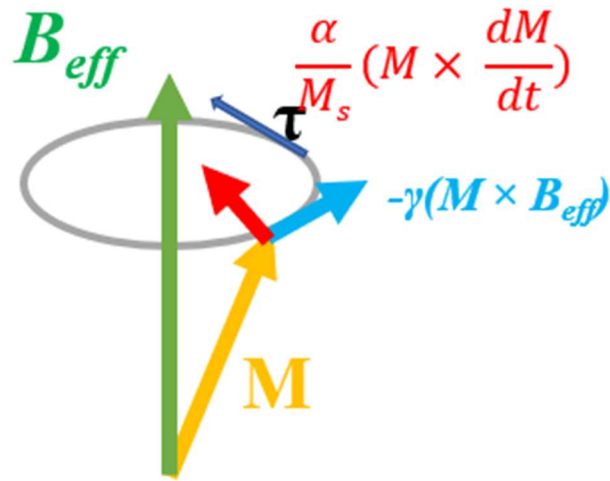


Figure 10. Schematic illustration of the Landau-Lifshitz-Gilbert equation. The magnetization M precesses along the applied field due to the torque ($M \times B_{\text{eff}}$). The Gilbert damping is responsible for the relaxation of magnetization towards the equilibrium state, due to which the magnetization follows a helical trajectory around B_{eff} .

The origin of damping in magnetic materials is still not completely understood. In general, the damping can be understood through relaxation mechanisms which are divided into intrinsic and extrinsic categories. Direct coupling of magnons to be phonons in the lattice via spin orbit interaction are intrinsic contributions to the damping whereas scattering processes from electrons leading to magnon-magnon scattering are extrinsic processes.

2.4 Magneto-Optical Phenomena

Light is a transverse wave made of electric and magnetic fields oscillating perpendicular to each other and the direction of propagation. By convention, the polarization of

an electromagnetic wave is defined to be the direction of the electric field vector. There are three different bases of light polarization, linear polarization is when the electric field is confined to a plane along the direction of propagation, circular polarization is when the electric field vector does not change strength but rotates about the propagation axis tracing a circle in a plane perpendicular to the direction of travel, and elliptical polarization in which the electric field vector traces out an ellipse.

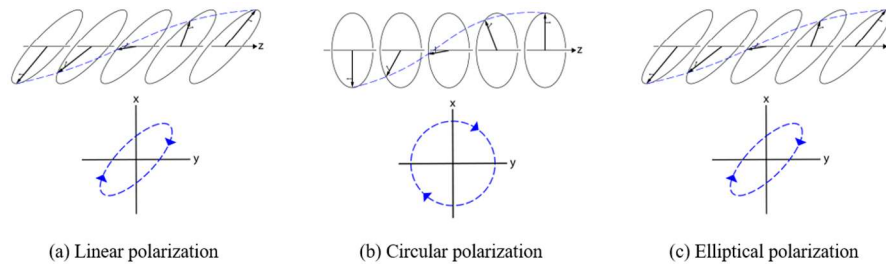


Figure 11. The three bases for the two states of polarized light. The electric field vector traces out the shape in a plane normal to the direction of propagation.

In this dissertation, linear polarized light will be mainly discussed, which can be regarded as the sum of a right circularly polarized beam and a left circularly polarized beam of equal amplitude and the orientation angle θ is the result of the relative phases of the two beams as shown in *Figure 12*.

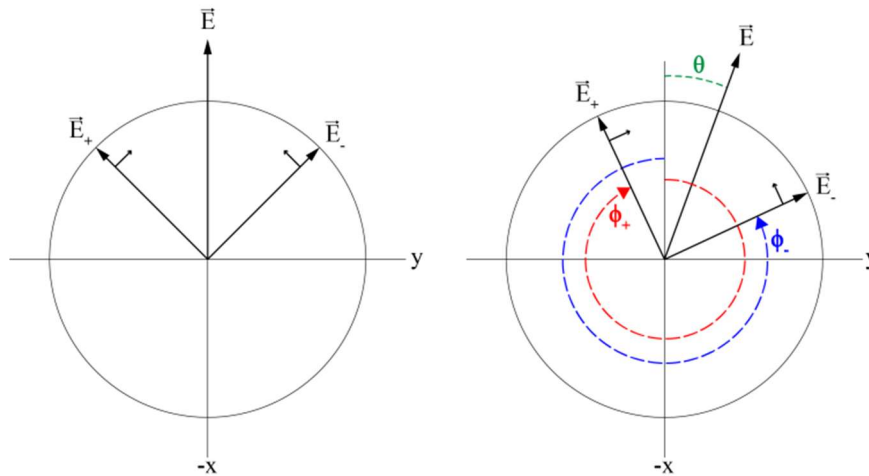


Figure 12. Linearly polarized light can be decomposed into two circular polarized components. A phase shift between the components will cause the plane of polarization of the light to be rotated by an angle θ .

Magneto optic effects arise when light interacts with a medium that is inside a magnetic field. These effects have been studied for nearly 200 years and have had a profound impact on the development of modern physics. The interaction of light with matter is affected by the magnetic state of the medium and involves the electronic structure of the matter. Such interaction between electromagnetic radiation and magnetically polarized materials results in ‘Magneto-Optic’ effects. In 1845, M. Faraday observed the rotation of the polarization plane of a linearly polarized light propagating through a piece of lead-borosilicate glass placed in a magnetic field, whereas J. Kerr observed the rotation of the polarization plane of a linearly polarized light upon reflection from the surface of a piece of *Fe* with either in plane or perpendicular to plane polarization in 1877^[84, 85]. These observations indicated the intimate relationship between the magnetic field and the linearly polarized light.

In addition, the Faraday effect, and its counterpart in reflection, the Magneto-Optical Kerr Effect (MOKE), are widely used to detect the magnetization of materials^[86, 87]. The MOKE offers a unique tool for the determination of the surface magnetization of thin films. Materials with large magneto-optic responses are widely being used in Faraday rotators, mode-conversion waveguides, and optical data storage^[87].

The light beam can be considered as an electromagnetic wave which can be linearly polarized. A linear polarized light is a wave with the electric field vector, \mathbf{E} , oscillating along a given direction, perpendicular to the propagating direction.

2.4.1 Magneto-Optical Faraday Effect (MOFE)

The MOFE is a magneto-optical phenomenon and reported on the polarization direction of linearly polarized light would undergo a rotation when passing through a transparent material with the application of a magnetic field along the direction of light propagation^[88], illustrated in *Figure 13*.

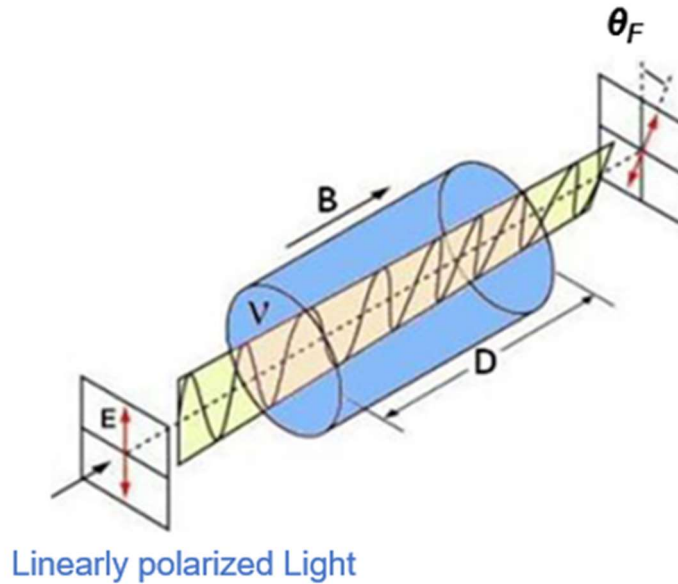


Figure 13. The MOFE. Linearly polarized light passing through a medium in a magnetic field along the direction of light travel will acquire a rotation of the plane of polarization. B is the strength of the magnetic field, D is the path length in the material, and θ is the total rotation angle. Figure adapted from Wikipedia.

The MOFE is described by, where the optical rotation (θ_F) of light is the product of the thickness of the material (D), the strength of the applied magnetic field (B), and the Verdet constant (V), which is a material dependent constant that depends upon the properties of the material as well we the ambient temperature, and the wavelength, λ , of the incident light^[89].

$$\theta = V \cdot D \cdot B \quad (16)$$

By convention, a positive Verdet constant corresponds to counterclockwise rotation when the direction of propagation is parallel to the applied magnetic field and clockwise when antiparallel^[90]. This leads to the important result, in contrast to natural optical

activity, that if a beam of light passes through and acquires a rotation θ , upon being reflected and passing through in the opposite direction that rotation will double 2θ rather than cancel.

2.4.2 Magneto-Optical Kerr Effect (MOKE)

The Magneto-Optic Kerr Effect (MOKE) is the study of the reflection of linearly polarized light by a magnetized sample surface subjected to a magnetic field, which was discovered in 1877^[91]. The material can be any magnetic material with a reflective surface; this includes metals, magnetic ceramics (ferrites), and magnetic semiconductors. This reflection can produce several effects including rotation of the direction of polarization of the light, introduction of ellipticity in the reflected beam, and a change in the intensity of the reflected beam.

The MOKE technique is a highly sensitive technique and important in the study of magnetization dynamics of magnetic films and materials. It can measure the change of the polarization states of the incident light when reflected from the surface of a magnetic material. Linearly polarized light experiences a rotation of the polarization plane (Kerr rotation θ_k) and a phase difference between the electric field components perpendicular and parallel to the plane of the incident light (Kerr ellipticity ϵ_k). It has wide applications in the study of magnetism due to a combination of straightforward implementation and versatility^[92-94].

MOKE measurements are usually performed in one of three different configurations, which differ in the polarization direction of the incident light and applied magnetic field direction (details in *Table I*). There are three orientations of the magnetic field relative to the sample: (a). Polar, (b). Longitudinal, and (c). Transverse geometries, shown in *Table I*. Definition of MOKE geometries

MOKE geometry	Magnetic field orientation
Polar	Parallel to the plane of incidence, normal to the sample surface
Longitudinal	Parallel to the plane of incidence and the sample surface
Transverse	Normal to the plane of incidence, parallel to the sample surface

In the polar geometry, the sample's magnetization, \mathbf{M} , is parallel to the plane of incidence and normal to the reflecting surface (*Figure 14 (a)*). Polar MOKE is most frequently studied at near-normal angles of incidence and reflection to the reflecting surface. This is also the geometry used in my research and the direction of the light beam I used it normal to the surface plane.

In the longitudinal geometry, the magnetization, \mathbf{M} , is parallel to both the plane of incidence and the sample surface (*Figure 14 (b)*). For the transverse MOKE geometry, the magnetic field is normal to the plane of incidence (*Figure 14 (c)*). The different geometries change the amount of polarization rotation and ellipticity for a given sample and incident light. The effect on linearly polarized light in the longitudinal geometry is same as the polar, either a rotation of the polarization or an ellipticity is introduced upon

reflection. In the transverse geometry, however, the only effect on incident light is a change in reflectivity.

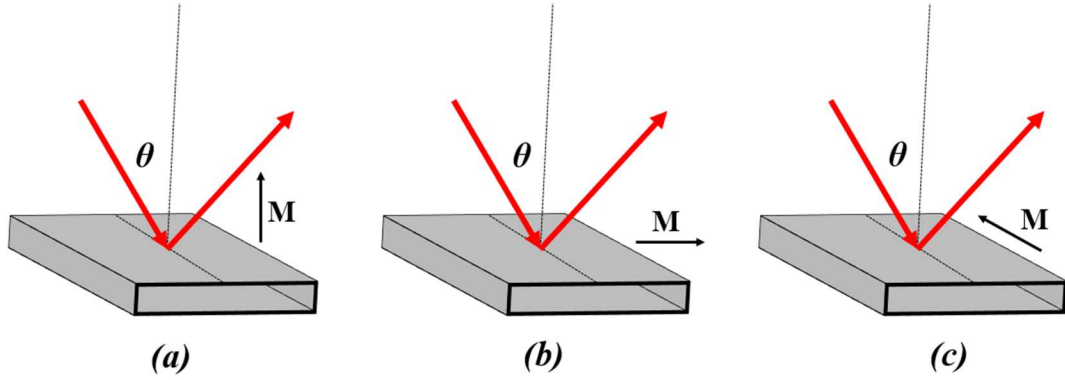


Figure 14. Schematic of the three different MOKE configurations: (a) Polar, (b) Longitudinal, and (c) Transverse MOKE geometries and the effect on arbitrarily polarized light incident at angle θ . The black and red arrows depict the magnetization component that is measured and the light propagation direction, respectively.

Mathematically speaking, magneto-optical effects arise from imaginary off-diagonal elements in the dielectric tensor of the material.

For a polar MOKE orientation, the dielectric tensor is as follows:

$$\frac{\epsilon}{\epsilon_0} = n^2 \begin{pmatrix} 1 & iQ & 0 \\ -iQ & 1 & 0 \\ 0 & 0 & 1 \end{pmatrix} \quad (17)$$

where Q is a magnetic parameter that is proportional to the strength of the magnetic field and dependent on the properties of the material. n is the average index of refraction of the material. The off-diagonal elements are what give rise to the changes in polarization by affecting the phase of the polarization components of light.

2.5 Coplanar Waveguide

A waveguide is a structure that can be used to transmit electromagnetic waves across some medium with relatively low loss. CPWs are a unique form of transmission line where all features are 2D and can be easily fabricated using photolithography techniques and are also the most frequently used planar transmission lines after microstrips. The waveguide consists of a center conductor strip and two ground conductor planes with variable widths. All three conductors are placed on the same side of a dielectric substrate, as illustrated in *Figure 15*.

C.P. Wen first proposed the CPW and carried out a quasi-static analysis of it using the conformal mapping method^[95]. CPWs can achieve lower dispersion via tight coupling between signal and ground conductors^[96]. CPWs provide better isolation than microstrips due to the G-S-G configuration which in turn allows for higher packaging density and smaller chip size but suffers from higher losses and have lower power handling capability compared to microstrips^[97]. To fully characterize a CPW, we need to know the effective dielectric constant (ϵ_{eff}) and characteristic impedance (Z_0). Resonance occurs in waveguides when the structure allows for the creation of a standing wave at certain frequencies.

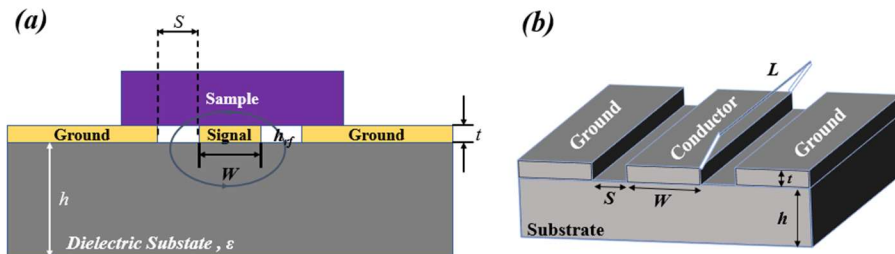


Figure 15. Illustration of the flip-chip orientation of a magnetic sample, shown in purple, placed face-down on a CPW, shown in gold. The width of the center conductor is given by W , and the gap between the center conductor and ground plane is given by S , with the thickness of the insulator underneath the top plane as t .

The propagation of electromagnetic waves along a CPW can be analyzed in terms of a distributed circuit model as long as the lateral dimension of the CPW are much smaller than the wavelength of propagating signals. Considering a short length of a uniform CPW with the resistance per unit length R , inductance per unit length L , conductance per unit length G and capacitance per unit length C , as shown in *Figure 16*. The voltage across R and L and current through G and C can be expressed as:

$$\begin{aligned} -dV &= (R + j\omega L) dl \cdot I \\ -dI &= (G + j\omega C) dl \cdot V \end{aligned} \quad (18)$$

where ω is the angular frequency. Then the second-order differential equation for the voltage is given by:

$$\frac{d^2V}{dz^2} = (R + j\omega L)(G + j\omega C)V = \gamma^2V \quad (19)$$

Thus, the propagation constant γ of a CPW is introduced by:

$$\gamma = \sqrt{(R + j\omega L)(G + j\omega C)} = \alpha + j\beta \quad (20)$$

where α is the attenuation constant and β is the phase constant. Two important properties of CPW, attenuation and dispersion, are determined by α and β .

The general solution is:

$$V = M_V \cosh(\gamma l) + N_V \sinh(\gamma l) \quad (21)$$

where M_V and N_V are constants to be determined. Similarly, we obtain

$$I = M_I \cosh(\gamma l) + N_I \sinh(\gamma l) \quad (22)$$

where M_I and N_I are constants to be determined.

Therefore, we get:

$$M_V \cosh(\gamma l) + N_V \sinh(\gamma l) = -Z_0 [M_I \cosh(\gamma l) + N_I \sinh(\gamma l)] \quad (23)$$

where we can find the characteristic impedance of the CPW can be expressed as:

$$Z_c = \sqrt{\frac{R + j\omega L}{G + j\omega C}} \quad (24)$$

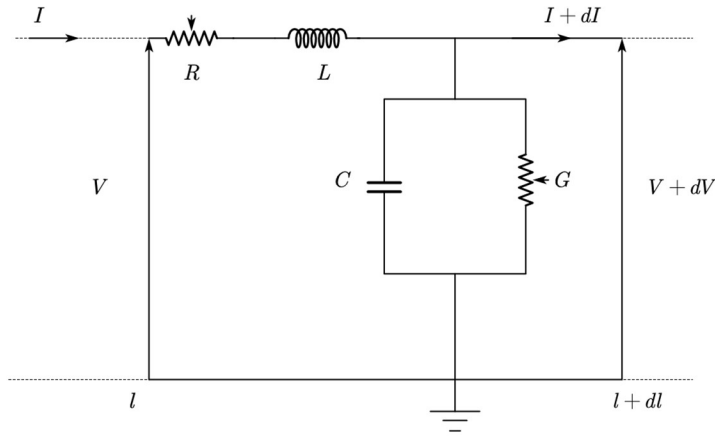


Figure 16. Distributed circuit model of a CPW.

As a building block towards the larger goal of quantum computing, this dissertation is focused on fabrication of suitable resonators for best performance. A high-quality factor, Q , is desired, so that the transmission line resonators used in this dissertation were

designed to minimize energy lost and maximize the coupling strength. The resonators are completely planar, and the pattern was transferred by means of wet etching. The majority of the resonators fabricated were characterized using a vector network analyzer (VNA). Information on the VNA, other apparatus, and procedures can be found in Chapter 4. Lastly, the results of our research are presented and analyzed in Chapter 5.

CHAPTER THREE

THIN FILMS STRUCTURES, DEPOSITION, AND CHARACTERIZATIONS

Thin YIG is a promising material for integrated spintronics or magnonics device. It is a ferrimagnet with an energy gap of 2.7 eV. The Curie temperature of YIG can range between 553 ~ 559 K^[95-97]. A brief introduction will be given in this dissertation and also the various results published over the last decades will be presented.

In the past decade, the field of spintronics/magnonics has become more and more attractive. Using magnons for information processing would allow for low dissipation data processing devices and hold the promise of complex functionality^[3, 5, 6, 98]. The use of ferromagnetic or ferrimagnetic materials bring to mind the possibility of non-volatile data storage or non-volatile programmability. From the point of view of commercial lithography, this is not a problem at all. The challenge, however, is on the materials side. Thin film metallic ferromagnets can easily be patterned with the required resolution as has been demonstrated in MRAM processing. Nevertheless, in order to realize complex magnonics, it is necessary to have very low damping and very long spin relaxation lengths in the ferromagnet of choice. YIG is well known and well-studied since several decades and as a bulk or thick film material can exhibit FMR linewidths of 15- μ T (FWHM) at 9.6 GHz and show a damping of $\alpha < 3 \times 10^{-5}$ ^[99].

In the following, three different growth methods are described and compared in terms of results, namely high temperature PLD, room temperature sputtering with

subsequent annealing, and room temperature PLD with subsequent annealing. It is noteworthy that in all of these experiments GGG has been used as a substrate. Besides the fact that the garnet structure of GGG is favorable for YIG growth, the lattice constant of the GGG substrate (1.2383-nm) is very close to the YIG bulk value of 1.2376-nm.

This chapter discusses some general information about common materials used for spintronic devices. Materials are chosen to enhance various operating characteristics of a device, such as higher Neel and Curie temperatures for higher temperature operation, or a pairing of a FM and insulator material that gives a stronger coupling.

3.1 Introduction to YIG Spintronics and Thin Film Growth and Characterization

The goal of spin-electronics (known as spintronics) is to create and manipulate spin currents for spintronics applications. Investigating the interactions between electron spin and solid-state environment is the main objective of spintronics and using what's been obtained to develop the next generation of memory devices. Incredible advancements in data storage, non-volatility, low power consumption, higher data processing rate, and excellent performance has evolving from that. The research in this dissertation will enhance the interest in the field of spintronics.

The recent development of spintronics and magnonics creates a demand for micrometer thick YIG films with high crystalline quality that continue to exhibit extremely low Gilbert damping. YIG has been grown by several techniques with Liquid Phase Epitaxy (LPE) being the most successful at obtaining the highest quality for micrometer

thick^[100-102]. Radio-frequency (RF) sputtering followed by either in situ annealing or post-growth annealing has attracted considerable interest^[103-105]. Within this dissertation, we carried out the detailed investigation of the structural, magnetic and FMR properties of micrometer thick YIG films for a better understanding of its characteristics and future optimization.

This chapter first presents an overview of the unique non-reciprocal behavior of garnet materials, and then devoted to the theoretical background of the magnetization dynamics and interface effects that are the foundation of this dissertation. In this first part of this chapter, the growth method and the crystal structure and magnetic properties of Yttrium Iron Garnet are described. Then the fundamental principles of the magnetization dynamics and the Landau-Lifshitz-Gilbert equation governing the precessional motion of the magnetization in the presence of a magnetic field are introduced. The basic principles of the ferromagnetic resonance, spin-pumping effect and current induced spin transfer torque is discussed in the following section.

3.1.1 Crystal Structure and Magnetic Properties of YIG

Yttrium Iron Garnet, YIG is a ferrimagnetic insulator and discovered by F. Bertaut and F. Forrat in 1956^[106, 107], has been widely employed to study magnetization dynamics in magnetic solids due to its magnetic properties. It is known that magnetization damping in YIG is extremely small, $\alpha \approx 3 \times 10^{-5}$ ^[59, 60]. Additionally, it has negligible optical absorption at infrared wavelengths^[108], low spin-wave dampening^[60], microwave

filtering capability^[109], and promising magneto-optical properties^[110]. Furthermore, its high Curie temperature of 545 K^[111] allows for experimental to be conducted at ambient temperature.

A total of 160 ions, including 24 Y³⁺ cations, 40 Fe³⁺ cations, and 96 O²⁻ cations, are found in the 8 chemical formula units of Y₃Fe₅O₁₂ that makes up the YIG unit cell. The lattice constant a is $12.376 \pm 0.004 \text{ \AA}$ ^[107, 112]. In each formula unit of YIG, there are three dodecahedral (c site), two octahedral (a site) and three tetrahedral sites (d site). The Y³⁺ ions occupy the dodecahedral sites (c sites), each site being surrounded by eight O²⁻ ions, that forms an eight-cornered twelve-sided polyhedron. 24 Fe³⁺ occupy tetrahedral sites (d sites) and are surrounded by four O²⁻ ions forming tetrahedral symmetry. The 16 Fe³⁺ occupy the octahedral sites (a sites) and are surrounded by six O²⁻ ions forming octahedral symmetry. The O²⁻ ions sit on h sites, each being at a point where the corners of one octahedron, one tetrahedron, and two polyhedrons meet. Thus, each O²⁻ ion is surrounded by one d site Fe³⁺ ion, one a site Fe³⁺ ion and two c site Y³⁺ ions.

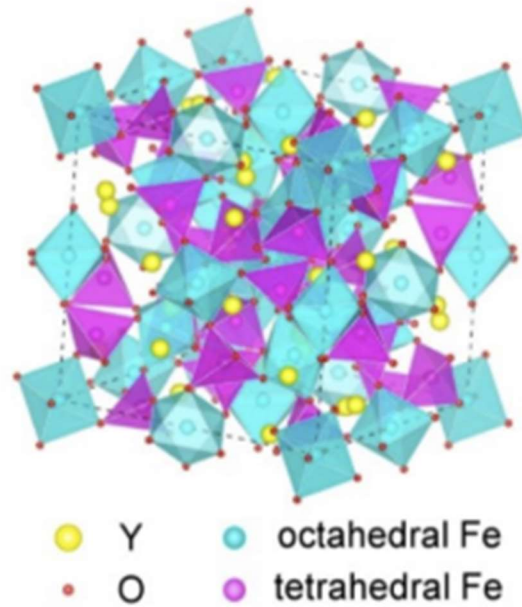


Figure 17. Crystalline structure of Yttrium Iron Garnet ($\text{Y}_3\text{Fe}_5\text{O}_{12}$)^[113]. The unit cell of YIG has cubic structure containing eight chemical formula units of $\text{Y}_3\text{Fe}_5\text{O}_{12}$ with 160 ions in total. The Y^{3+} ions occupy dodecahedral sites (c sites), Fe^{3+} occupy tetrahedral sites (d sites) and 16 Fe^{3+} occupy the octahedral sites (a sites). The magnetization in YIG originates from the super-exchange interactions between 16 Fe^{3+} ions on a sites and 24 Fe^{3+} ions on d sites.

In *Figure 17* the crystalline structure of YIG is shown. Since Y^{3+} is diamagnetic, the magnetization in YIG originates from the super-exchange interactions between 16 Fe^{3+} ions on *a* sites and 24 Fe^{3+} ions on *d* sites. *Figure 17* shows the Fe^{3+} -ions form two sub-lattices: Fe^{3+} -ions are sitting on octahedral and tetrahedral sites^[107, 111]. The sites differ in the configuration of neighboring O^{2-} -ions which are responsible for the superexchange interaction of the magnetic ions. Each of the Fe^{3+} -ions carries a magnetic moment of $5\mu_B$. Two Fe^{3+} -ions are sitting on the sites of the octahedral sub-lattice, whereas

there Fe^{3+} -ions are sitting on the sites of tetrahedral sub-lattice. The two sub-lattices are oriented anti-parallel, consequently, they partially compensate each other: the total YIG magnetic moment is $5\mu_B$. These properties make it particularly suitable for studies of spin waves and magneto-optical effects, as well as for blooming studies of magnetic insulator-based spintronics. The intrinsic damping constant α for YIG is two orders of magnitude smaller than that in transition metal compounds such as Permalloy (Py) which are the other common materials in current spintronics devices.

Due to similar lattice parameters, yttrium iron garnet thin films are normally grown on (111) gadolinium gallium garnet ($\text{Gd}_3\text{Ga}_5\text{O}_{12}$, GGG) substrates. GGG has a cubic crystalline structure with eight formula units per unit cell and a lattice constant of $a = 12.383 \text{ \AA}$ ^[112]. Thus, the lattice mismatch is very small which allows for growth of the YIG films on GGG substrates.

3.1.2 Deposition of Thin Films

YIG thin film is expected to be an ideal candidate for modern miniature microwave devices because of its low magnetic loss at microwave frequencies^[60, 114]. There are many methods to grow YIG thin films in different environments; for example, LPE is usually employed to prepare high-quality epitaxial YIG thin films on GGG substrate^[115, 116]. Later, it was demonstrated that the pulsed laser deposition (PLD) is a better suited technique to deposit epitaxial YIG films on GGG^[117]. In addition, RF sputtering was proved to be one of the preferred methods for depositing YIG films^[117-122]. YIG thin

films used in this dissertation were grown by RF magnetron sputtering on GGG <111> single crystal substrates, at room temperature. The films were ex-situ annealed at a high temperature (700 ~ 900 °C) in air atmosphere for about 8 hours. The annealing was carried out on a new piece of sample each time^[123].

3.1.2.1 Magnetron Sputtering

Sputtering is a common physical vapor deposition (PVD) of thin films on the substrates by using plasma. In this dissertation, all sputtered samples were made by magnetron sputtering technique in an Ar gas atmosphere, and the base pressure of the sputtering chamber is of the order of 10^{-7} Torr. Magnetron sputtering was chosen over conventional sputtering because the sputtering yield of conventional sputtering is very low and causes the structural and heating damage to the substrate. However, these issues are overcome by the use of magnetron sputtering. In magnetron sputtering, a magnetic field perpendicular to the applied electric field is applied so that electrons are trapped just above the target in a helical path. This results in increased electron-Ar⁺ collisions close to the target, thereby increasing the sputtering rate, while at the same time decreasing electron collisions with the substrate^[124].

Figure 18 depicts a schematic illustration of a sputtering system. The sputtering deposition chamber consists of two electrodes in a vacuum with an external high voltage power supply. The material to be deposited, is called the target and acts as the cathode, the substrates are placed on the sample wheel which is earthed.

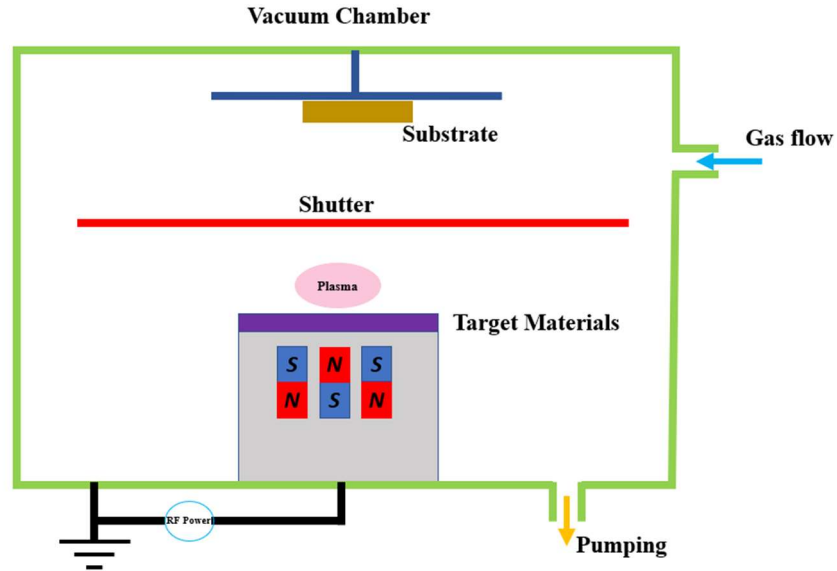


Figure 18. A schematic diagram of a rf-sputtering system. A RF voltage is applied between cathode (target) and anode (the target can), after introducing sputtering gas to the evacuated chamber. The argon atoms are ionized due to the accelerated electrons between the electrodes resulting in a plasma. Due to the bombardment of the ionized ions on the target, materials are ejected from the surface of the target and get deposited on the substrate.

An energy source applies DC/RF voltages across the electrodes to ionize the Ar gas to create and maintain plasma, followed by removal of the target material by ion bombardment and ejection of material from the target to the substrate.

The sputtering gas is introduced into the vacuum chamber. To sputter an atom from the target, momentum transfer from the ion-induced collision must overcome the surface barrier, given by the surface binding energy. When a DC/RF voltage is applied between the cathode and anode, an electric discharge is produced. This leads to the partial ionization of the gas and these ions when strike the target with sufficient energy cause

ejection of surface atoms from the target and deposition onto the substrate. During this, the ionized gas and the free electrons are accelerated by the voltage and continue to collide, causing further ionization of the gas. Finally, a breakdown condition is reached, and the plasma is stabilized.

Sputtering methods can be classified as DC and RF sputtering depending on the material to be deposited. DC sputtering is used for the metal deposition whereas RF sputtering for the deposition of thin films of insulator. In DC sputtering, a DC voltage is applied to create plasma between the electrodes. In RF sputtering, a voltage oscillating at RF, typically around 13.56 MHz, is applied to bias the electrode and to sustain the glow discharge. As the current is alternating, this will prevent buildup of a surface charge of positive ions on the front side of the insulator. On the positive cycle, electrons are attracted to the cathode, creating a negative bias and on the negative cycle, ion bombardment of the target to be sputtered continues. The sputtered atoms are ejected, which are then deposited on the substrate. For magnetron sputtering, permanent magnets are placed beneath the target so as to confine the plasma by the Lorentz force. There is a shutter system which allows to grow multilayers of different materials.

We control the sample wheel and the shutter position remotely by using software. Our thin film of YIG were grown on <111> GGG substrates by RF magnetron sputtering. The deposition rate is greatly influenced by the RF power, pressure, temperature, and the flow of sputtering gas. During the deposition of YIG films, the system had a base pressure of 2×10^{-8} Torr in the main chamber, argon flow rate was 20 SCCM (standard cubic

centimeters per minute) and the RF power was maintained at 50 W at 13.56 MHz. There is an impedance-matching network between the power supply and discharge chamber, which is tuned to get zero reflected power back to the source. The target and inductance in the matching network are always water-cooled.

The thickness of the deposited films (Py, YIG, Cu, and SiO₂) in the research that resulted in paper I of this dissertation was in the range of 10-nm ~ 3- μ m. The film deposition rate can be measured and then the film deposition time was calculated based on the deposition rate in order to get the desired film thickness.

3.1.2.2 Annealing

Deposition processes use room temperature needs the annealing promotes the necessary recrystallization. When growth is performed at elevated substrate temperatures, the annealing step usually can be avoided.

The amorphous YIG films in order to turn them into crystalline YIG along the GGG crystalline plane. The samples are first cleaned with isopropanol and acetone prior to annealing. The samples are immediately placed in a tube furnace, where they are annealed for two hours at 850 °C in the open air. In order to prevent strain on the films, the heating and cooling cycles are performed at a pace of 10 °C per minute.

3.1.3 Characterizations of the YIG Thin Film

For the YIG films presented in this dissertation, the static magnetic properties of the YIG films were measured by a superconducting quantum interference device (SQUID) and the dynamic properties of the films were determined through (1) polar angle dependent ferromagnetic resonance (FMR) measurements using an X-band rectangular microwave cavity with a resonance frequency of 9.5 GHz and (2) frequency-dependent FMR measurements using a broadband vector network analyzer FMR (VNA-FMR) spectrometer. For (1), field modulation and lock-in detection techniques were used to increase the sensitivity of the FMR measurements. For (2), a CPW was used to provide microwave magnetic fields to the YIG films.

3.1.3.1 SQUID Technique

This dissertation is concerned with the magnetic behaviors of a variety of different materials, on a bulk, molecular, and atomic scale. As such, care had to be taken when choosing a suitable magnetic sensor to gather data. There are numerous experimental instruments commercially available which typically gather data through the detection of either magnetic fields or magnetic flux^[125]. Each device is generally specialized to detect a specific magnetic property and as such the instrument used in a given experiment is dependent on the information we want to learn about a particular sample. Table I outlines some key magnetic properties and the corresponding experimental instruments which can be employed to measure these properties.

Table II. Key magnetic properties and corresponding methods of measurement.

Magnetic Property	Description	Measurement Method
Intrinsic Coercivity	Measure of a magnet's resistance to demagnetization	Hysteresisgraph, Vibrating sample magnetometer (VSM) and SQUID magnetometer
Magnetic flux	Measure of magnetic output; related to magnetic moment	Helmholtz or Search Coil and Fluxmeter
Magnetic Field Strength, flux density	Measure of the magnetic (flux) output per unit area	Gaussmeter
Reversible Temperature Coefficients	Indicate how the magnetic characteristics change with temperature	Hysteresisgraph, VSM or SQUID
Field Distribution	Measure of the distribution of the flux	Magnetic Field Scanners

The SQUID magnetometer is the most attractive magnetic sensor to measure very small magnetic moments with high sensitivity. It does not directly measure the magnetic moment of the sample and is in fact an extraction magnetometer^[126]. In order to allow for the application of large magnetic fields and a wide range of temperatures, a very sophisticated system of superconducting pick-up coils and wires is adopted to transfer a current signal from the sample to the SQUID detect.

The magnetized specimen is moved up and down through superconducting pick-up coils; known as flux transformers, which are located outside of the sample chamber. The change in magnetic flux generated by the sample motion induces a current to flow within the pickup coils. The current is then carried along superconducting wires to the SQUID input coil.

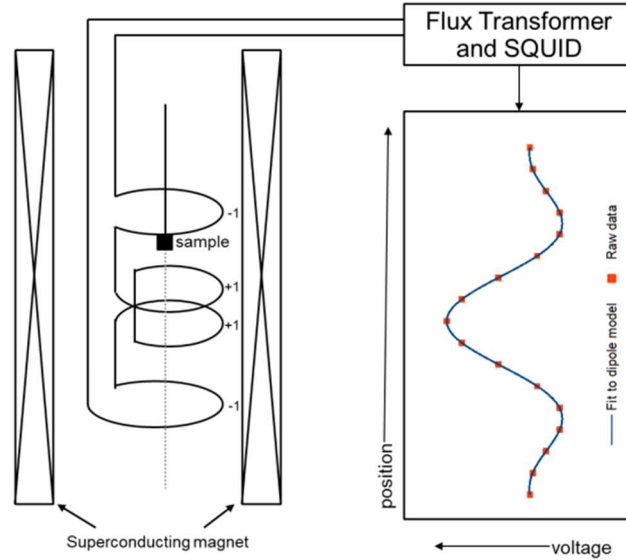


Figure 19. Pick-up coil geometry and theoretical response signal of ideal dipole versus scan length in a MPMS SQUID magnetometer.

It combines the physical phenomena of flux quantization^[127] and Josephson tunneling^[128]. A Josephson junction is the heart of squid technology in which current flows between two superconductors separated by a thin insulator through quantum tunnelling. In 1962, B. Josephson observed that the supercurrent tunneling through a superconductor-insulator-superconductor junction should be a periodic function of the phase difference between the superconducting wave-functions on either side of the junction^[128, 129]. *Figure 20* shows the schematic of a Josephson junction. In the Josephson junction, the supercurrent I_s passing through the junction is related to the relative phase difference δ across the junction and the critical current of the junction, I_0 as:

$$I_S = I_0 \sin \delta \quad (25)$$

$$\delta = \theta_1 - \theta_2$$

where δ is the difference between the phases θ_1 and θ_2 of the two superconductors.

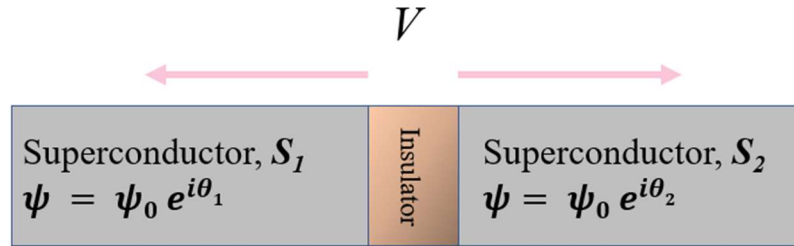


Figure 20. Schematic of a Josephson junction. It consists of two superconductors separated by a thin insulator through which cooper pairs can tunnel and leads to the flow of supercurrent. Ψ is the wavefunction of the superconducting state in the left and right superconductors, and θ_1 and θ_2 are the phases.

3.1.3.2 FMR Experimental Setup

FMR spectroscopy is an important technique for the characterization of ferromagnetic samples, and probe static and dynamic properties of magnetic materials. The technique relies on measuring the microwave absorption associated to the precession of the magnetization, and can be used to extract valuable information about material parameters such as e.g. the effective magnetization, anisotropies and the magnetodynamic damping^[130].

In an FMR experiment, a static magnetic field is applied in combination with an orthogonal microwave magnetic field. The microwave magnetic field will induce a precession motion of the electron spins, provided that the frequency of the applied

microwave field coincides with the FMR frequency. As the resonance frequency is determined by the effective magnetic field, one can either vary the frequency of the microwave field at a fixed value of the external field or keep the microwave frequency fixed and sweep the magnitude of the external field in order to change the resonance frequency. An experimental setup used in this dissertation, named VNA-FMR is presented in the following section.

VNA-FMR is frequently used to characterize the magnetization dynamics in the microwave frequency range. In FMR, the magnetization of the ferromagnet is resonantly excited by RF magnetic field H_{RF} , which oscillates at microwave frequency f_{drive} and applied in the direction transverse to the external magnetic field H_{ext} . The sample absorbs the microwave power at the resonance when the drive frequency f_{drive} coincides with the resonance frequency f_r of the magnetization.

FMR provides a number of magnetic parameters related to the high-frequency behavior of magnetization, including the damping constant^[131, 132] α , g -factor^[131], and exchange coupling^[133-135], among others, as well as magneto static properties. The VNA-FMR approach, which operates over a broad range of frequency and yields FMR parameters from typical microwave S parameter measurements versus frequency and field, is an essential tool for research on magnetic materials and spintronic devices^[136-139]. This section will provide a detailed introduction to the experimental VNA-FMR system that was used for this dissertation.

The signal-to-noise ratio of the VNA-FMR technique is high and it covers a wide range of frequencies^[137, 140-142]. After reaching the investigated sample, the incident wave will be reflected and/or transmitted (*Figure 21*). A torque will induce a spin to precess around a magnetic field when it is in the presence of a magnetic field at the Larmor frequency, which is equal to γH .

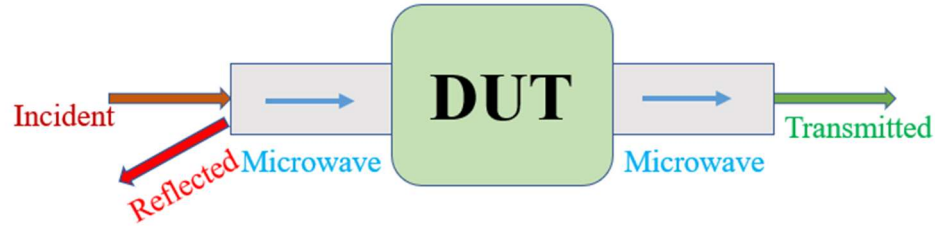


Figure 21. The incident wave will be reflected and/or transmitted after entering the device under test (DUT)

By analyzing the reflectance/transmittance, which is the ratio of reflected, transmitted power to that of incident, we can find the scattering parameters (S_{11} , S_{22} , S_{12} , S_{21}), from which we can extract the properties of the sample. *Figure 22* shows four S-parameters corresponding to a two-port DUT.

$$\begin{aligned} b_1 &= S_{11} a_1 + S_{12} a_2 \\ b_2 &= S_{21} a_1 + S_{22} a_2 \end{aligned} \quad (26)$$

where S_{11} and S_{22} are the reflection coefficients at the port 1 and port 2 respectively, whereas S_{12} and S_{21} represent the transmission coefficients. So, a microwave leaving the DUT is a linear combination of the microwave incident on the DUT.

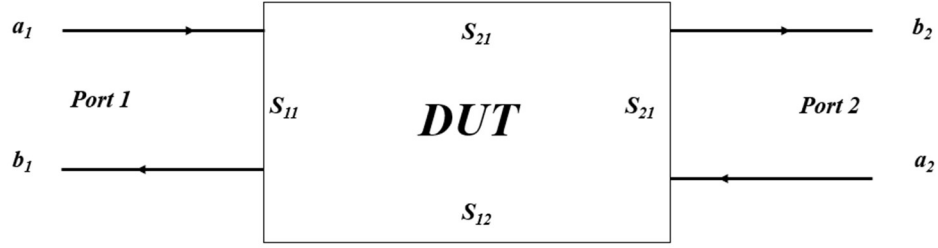


Figure 22. Two-port device S-parameters model

For the FMR measurements, we can sweep the microwave excitation frequency at a fixed bias magnetic field or at fixed excitation frequency, the static external magnetic field can be swept to achieve the resonance condition. On the one hand, by varying the microwave frequency at a fixed static field, extracts the FMR absorption profile from standard S parameter measurements, and obtains a FWHM (full width at half maximum) frequency swept linewidth Δf_{VNA} from the response. On the other hand, by sweeping the external magnetic field at a fixed microwave frequency, extracts the FMR absorption profile from standard S parameter measurements, and obtains a FWHM (full width at half maximum) field swept linewidth Δf_{VNA} from the response.

A block diagram of the VNA-FMR spectrometer built in this dissertation is illustrated in *Figure 23*. The sample under test (SUT) is placed on top of a CPW that connected to port 1 and 2 of a VNA to measure the transmission coefficient, i.e., S_{21} . The SUT used in this dissertation is a film stack of YIG (3- μm)/Py (10-nm) deposited on a transparent GGG substrate, for the purpose of demonstrating the magneto-optical effects within the FM insulator (YIG) and FM metal (Py) films and the PSSW modes excited by the exchange coupling between the YIG and Py thin film.

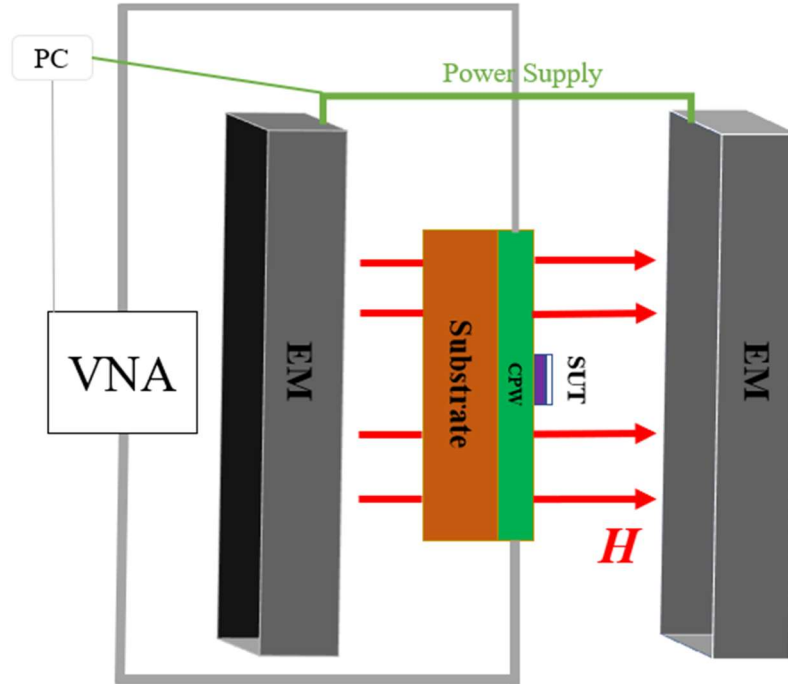


Figure 23. Block diagram of the VNA-FMR spectrometer built in this dissertation. Each functional block is labeled as follows: VNA: vector network analyzer, CPW: coplanar waveguide, SUT: sample under test, EM: electromagnet, and PC: personal computer. The EM generates a DC bias field H perpendicular to the CPW.

It can be operated in either the frequency sweep mode or field sweep mode. H is first set by the EM, and then the VNA measures S_{21} while the frequency is swept from 5.5 GHz up to 7.6 GHz with a step of 10 MHz; thus, each single sweep contains 211 data points of S_{21} taken under a constant H . The Raw S_{21} parameter contains both the non-magnetic background and the magnetic component, i.e., the FMR signal of interest. In addition, the raw FMR signal shows a significant frequency dependence the stimulus signal propagating from port 1 to the SUT and the FMR signal from the SUT to port 2 both undergo frequency dependent decay and phase rotation associated with the coax

interconnects. The standard algorithm for subtracting the nonmagnetic background and normalizing the frequency dependence is:

$$S_{21}^{FMR} = \frac{S_{21} - S_{21}^{NM}}{S_{21}^{NM}} \quad (27)$$

where S_{21}^{FMR} is the FMR signal of interest and S_{21}^{NM} is the nonmagnetic background. The most common method for determining S_{21}^{NM} is to measure S21 under the application of a large enough H to expel all the magnetic responses outside of the relevant measurement frequency range.

The VNA-FMR can also be operated in the field sweep mode. The measurement sequence of this operation mode used in this dissertation is basically the same as for the frequency sweep mode but with different measurement parameters for acquiring S21. H is first set by the EM, and then the VNA measures S21 while the frequency is swept from 5.5 GHz up to 7.6 GHz with a step of 10 MHz; thus, each single sweep contains 211 data points of S21 under a constant H.

The field sweep mode is much slower than the frequency sweep mode because it needs to set H and controlling H is so much lower than controlling the frequency. Therefore, the VNA-FMR operating in the field sweep mode is useful only in very limited cases.

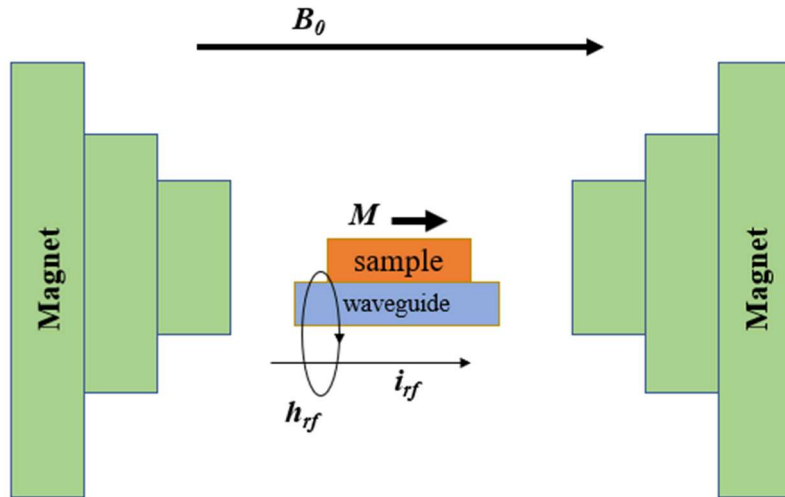


Figure 24. In-plane FMR, with the magnetization parallel to the thin film and the applied magnetic field.

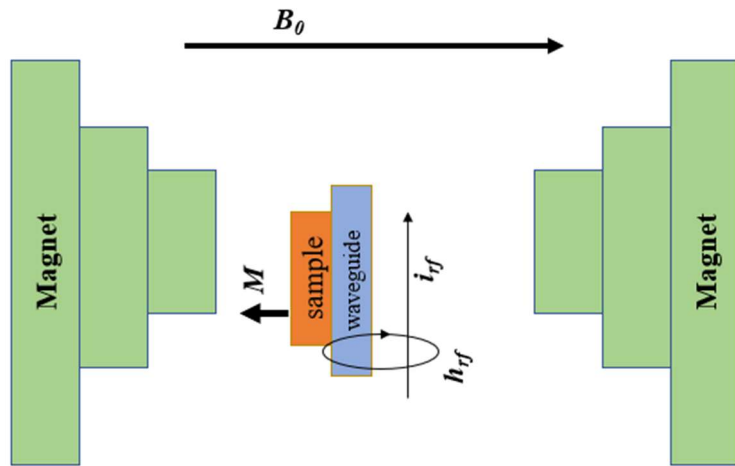


Figure 25. Out-of-plane FMR, with the magnetization perpendicular to the film and the applied magnetic field.

Excitation of FMR with waveguides carrying RF current i_{rf} , which produces a magnetic tickle field h_{rf} through the Oersted effect. The tickle field h_{rf} is used to excite the resonant precession of the magnetization may be produced by an RF current i_{rf} . The RF current is generated with a VNA and carried through a CPW. The CPW may be rotated with respect to the external magnetic field to conduct in-plane (IP) (shown in *Figure 24*) or out-of-plane (OOP) FMR (shown in *Figure 25*).

The impedance of the VNA and connectors used in the FMR setup are a standard 50 Ω . To avoid unwanted reflections and improve transmission, it is key to design the CPWs to have the same impedance of 50 Ω . Impedance mismatch reflects power and causes amplitude ripple at high frequencies, degrading the quality of the FMR signal and reducing the overall sensitivity of the measurement. Therefore, it is essential to calculate the characteristic impedance of a CPW design and bring it as close to 50 Ω as possible over the widest possible frequency band.

3.2 Magnetoelectric and Multiferroics

Over the past decades, there has been a revival of interest in materials or heterostructure that possess more than one ferroic parameter, largely due to the interest in studying the correlations between two or more ferroic orders^[143] as well as the possibility to demonstrate next generation devices using these correlations. Materials in which more than one order parameter coexist simultaneously are called multiferroics^[144, 145].

In the multiferroic family, only a few number of compound exhibit magnetic and electric order parameter simultaneously, i.e., ferromagnetic materials exhibit spontaneous magnetization and the spin ordering in the materials can be altered with an application of external electric field. Similarly, ferroelectric materials possess' spontaneous polarization and the ordering of the electrical dipoles in the materials can be controlled by applying magnetic field externally. Initially, the co-existence of ferromagnetic and ferroelectric in a single material was thought to be two independent properties. However, in some multiferroic, these two properties are coupled with each other, and this coupling interaction produces a promising functionality known as magnetoelectric effect. This coupling opens an extra degrees of freedom in the material which enables a control on the magnetic properties by applying an external electric field and vice-versa, providing a possibility to develop new devices based on these materials. In this dissertation, the focus is on multiferroics that possess both electrical and magnetic orders and the primary interest is the coupling between them.

From a scientific perspective the excitement behind magnetoelectric or the magnetoelectric effect in materials is the possibility to magnetically control a polarization and the inverse (electrical control of ferromagnetism)^[146]. Most of the research focus has been driven by the prospect of the electric field control of magnetism. While the magnetoelectric effect has recently become the focus of much theoretical and experimental investigation, the magnetoelectric effect was proposed long ago by P. Curie in 1894^[147] but was not experimentally verified for nearly 70 years later in Cr_2O_3 ^[148-150]. Most recent

investigations have reported improved multiferroic and ME properties in epitaxial layers of ME thin films such as BiFeO₃ grown on SrTiO₃[151], and in self-assembled multiferroic nanostructures such as CoFe₂O₄ nanopillars embedded in a BaTiO₃ matrix on SrTiO₃ substrates^[152]. These are potentially useful for integrated microelectronic materials that have the promise of reading a spin state as a direct voltage.

Electric control of magnetism has the potential for developing a new era of electronics devices^[153], such as nano-sensors and electrically tunable magnetic data storage in magnetoresistive random-access memory (MRAM). Overheating is a major problem in nano-electronic devices and electric field control requires much lower power compared to current driven magnetic devices, such as STT requires current densities $\sim 10^6$ A/cm² in MTJ with MgO and AlO_x tunnel barriers^[154]. Applied electric fields have been shown to control a wide range of magnetic properties including the Curie temperature, magnetic anisotropy, surface magnetization, exchange bias, and the spin polarization. Electric fields are either supplied via applied voltages, or alternatively by means of an adjacent ferroelectric. The mechanism behind electric control of magnetic properties arises either by induced strain from the piezoelectric materials or by means of polarization charge induced effects. The electric control of magnetism has been largely based on the elastic strain of the piezoelectric materials^[155-158]. The disadvantage of the piezoelectric strain-based control of a thin magnetic film is that it is constrained by the substrate. This dissertation focused on mechanisms that are not strain induced, but charge induced ME effect, which has been observed in multiferroic materials.

Due to theoretical physics and potential multifunctional applications, multiferroic materials – those that exhibit two or more ferroic orderings – such as ferroelectricity, ferroelasticity, and ferromagnetism – have attracted a great deal of research attention. Multiferroic materials are intriguing not only because they possess both magnetic and ferroelectric properties, but also because the magnetoelectric coupling results in increased utilization. Due to the low magnetoelectric coupling strength, the employment of these materials in switching applications remains a major problem.

The possibility of manipulating one ferroic property with the conjugate field of another is made possible by the combination of ferroic orders in the multiferroic materials. The ME effect, which refers to the possibility of changing the orientation of magnetization using an electric field, is especially interesting (*Figure 26*). Depending on the order parameter that is being impacted by the applied field, the ME effect is classified as “direct” or “inverse”. The ferroelectric polarization P that appears when exposed to a magnetic field H is known as the direct ME effect. This is denoted by ME_H and given by $P = \alpha H$, where α is the magnetoelectric coupling constant. The appearance magnetization M upon exposure to an electric field E is termed as the inverse ME effect, designated as ME_E and given by $M = \alpha E$. The ability to control magnetization by the electric field is particularly intriguing because it has the potential to significantly reduce power consumption and enable device miniaturization. Unlike conventional electronics, which only use the electron’s charge, spintronic devices combine the electrical and magnetic properties

of the electron by taking advantage of both the charge as well as the spin degree of freedom.

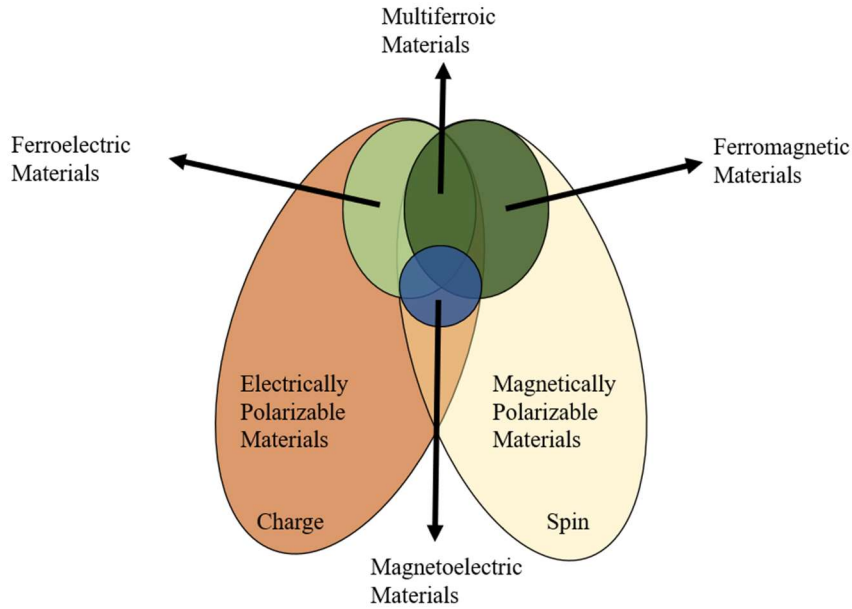


Figure 26. Schematic diagram for a multiferroic and magnetoelectric ordering in materials controlled by ferroelectric and ferromagnetic behaviors of the materials.

The capability to control magnetization is a key component in the creation of spintronic devices. It is technically challenging and requires a lot of power to generate a magnetic field that is strong enough to switch the high coercivity materials on small length scales. It is challenging to have reproducible control of magnetization because of the energy loss caused by the current flow in magnetic field assisted switching. Therefore, in order to solve the issues of today's modern technologies as well as advance the field of information technology, new paradigms are needed. In this regard, the potential

utilization of an electric field for reversible magnetization state switching appears to be a very attractive alternative to current driven read head technology. Additionally, the development of multifunctional spintronic devices is anticipated to benefit from it. Technically speaking, it is easy to generate energy efficient and fully switchable electric fields on small length scales. Naturally, the materials that may offer such an electric field assisted regulation of magnetization should also have ferromagnetic and ferroelectric characteristics. The best materials to use in these applications are consequently magnetoelectric multiferroics.

The naturally occurring single-phase compounds and the engineered composite multiferroics are the two main types of ME multiferroic materials. A number of breakthroughs and consistent advancement over the past decades have greatly broadened and strengthened our understanding of multiferroic physics, which is further extending the study frontier in this interesting topic. Sooner or later, more multiferroic materials will be offered, and improved magnetoelectric performance will make the applications practical.

Magnetoelectric physics and material research progressed at a rather modest pace throughout the 20th century. On the one hand, the measured magnetoelectric performance was subpar and magnetoelectric materials were scarce and inactive. Magnetoelectric theories, on the other hand, were primarily phenomenological and lacked elements of contemporary electronic theory founded on quantum mechanics. Ferroelectricity's contemporary electronic theory was not developed until the 1990s^[159, 160]. Multiferroics, which refers to the coexistence of multiple ferroic orderings in a single-phase material^[161], is a

new term that Schmid introduced in 1994. Later on, two unexpected breakthroughs, which both happened in 2003, signified the end of the long incubation period. The first was the finding of significant magnetization and considerable ferroelectric polarization in BiFeO₃ thin films at room temperature^[151]. A single-phase magnetoelectric compound with good multiferroic performance and possible room temperature applications was finally discovered. The second material is TbMnO₃, which developed only at extremely low temperatures (below 28 K)^[162] and has a weak polarization (~ 0.1% of that of BiFeO₃). The TbMn₂O₅^[146] and hexagonal HoMnO₃^[163] were discovered in the following year. TbMn₂O₅ exhibits a significant magnetoelectric coupling, providing switchable polarization in the presence of a magnetic field. Contrarily, hexagonal HoMnO₃'s high ferroelectric Curie temperature (up to 875 K) is greatly valued for its magnetoelectric behaviors^[164].

CHAPTER FOUR

PROBING MAGNON-MAGNON COUPLING IN EXCHANGE COUPLED $\text{Y}_3\text{Fe}_5\text{O}_{12}$ /PERMALLOY BILAYERS WITH MAGNETO-OPTICAL EFFECTS

Magnons have been demonstrated to efficiently couple to cavity quantum electrodynamics systems including superconducting resonators and qubits^[165-169].

When it comes to investigating spin waves in a thin film, there are three primary types of modes (forward volume magnetostatic spin waves (FVMSW), backward volume magnetostatic spin waves (BVMSW), and magnetostatic surface spin waves (MSSW)) that can propagate depending on the direction of the magnetic bias field and its relative orientation to the spin wave propagation vector (*Figure 27*).

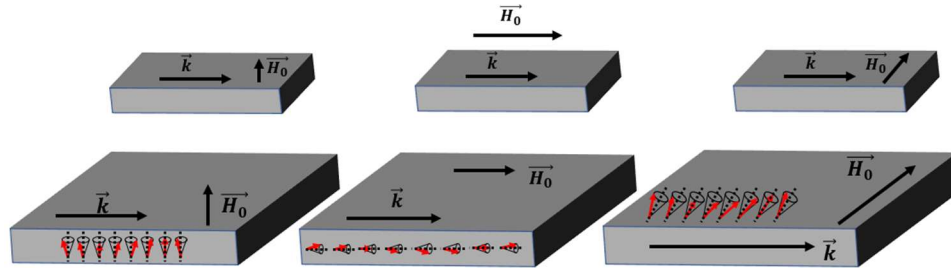


Figure 27. Configurations for propagation of FVMSW, BVMSW, and MSSW, respectively.

4.1 Experimental Setup

This work investigates the magnon-magnon coupling in YIG/Permalloy (Py) bilayers by a phase-resolved heterodyne detection method. We revealed the coupled magnon modes in the regime exhibiting the magnetically-induced transparency (MIT) effect,

i.e., the magnetic analogy of electromagnetically induced transparency (EIT)^[170-176], akin to a spin-wave induced suppression of FMR.

The magnetization dynamics are detected optically by the magneto-optical Kerr and Faraday effects for Py and YIG, respectively, by measuring the out-of-plane component of precessing magnetization using one single light wavelength at 1550-nm. This method is advantageous in the context of studying magnon-magnon coupling of hybrid insulator-metal systems, since it avoids the complication of using multiple wavelengths in the visible range for detecting respective metals and insulators.

In our system, the optical power used for the 1550-nm laser is between 6 ~ 8 mW and we detect a modulated voltage around 50 ~ 200 μ V. A heterodyne method is adopted to enable precessional phase extraction using a setup illustrated in *Figure 28*. A single microwave source was used to simultaneously modulate the detecting laser light (optical path) and drive the FMR of the sample (electrical path) with a CPW. The laser light was modulated at the microwave source frequency using an electro-optic intensity modulator. The modulated laser light can be polarized by either a fiber polarizer (used in combination with a polarization controller) or a free-space thin-film polarizer, before being focused onto the sample surface. We use an optical tap (~ 10%), a GRIN lens, and another free-space polarizer to monitor the polarization during the whole measurements. The focused light spot is set to ~ 40- μ m in this work. A microwave diode was used simultaneously to measure the inductive FMR absorption through the CPW.

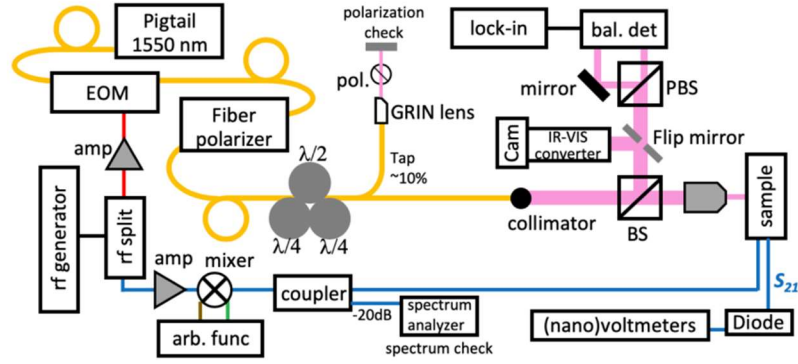


Figure 28. Schematic of the measurement setup. After the rf splitter, the optical path (upper part) contains amplifier, 1550-nm infrared laser module, electro-optic modulator (EOM), polarizer, polarization controller, beam splitter (BS) and focusing lens; the electrical path (lower part) contains amplifier, mixer, coupler, spectrum analyzer, diode, and nanovoltmeter. (PBS: polarizing beam splitter, Cam: camera, bal.det: balancing detector, arb,func: arbitrary waveform generator.)

For a heterodyne detection, the microwave signal along the electrical path was IQ-mixed with a low-frequency (100 kHz) signal provided by a waveform generator. The voltage amplitude, offset, and phase for the respective “I” and “Q” channels were optimized to ensure the power of the upper side-band of the microwave signal (which subsequently used for FMR excitation) far exceeds those of the central and lower side-bands (< 20 dB). We used a directional coupler (-20 dB), and a real-time spectrum analyzer to monitor the central and side-bands throughout the whole measurement. The resultant, out-of-plane, dynamical Kerr, and Faraday responses of the sample were then probed by the modulated light, sent into a balancing detector after polarization splitting, and analyzed by a lock-in amplifier. Avoiding the use of a VNA offers more flexibility in configuring the setup for different dynamic measurements^[177, 178]. The use of fiber-optical

components also increases the robustness against external vibrations as well as reduces the cost as compared with conventional VNA experiments^[179-183].

The commercial YIG films (from MTI Corporation) used in this work are 3- μm thick, single-sided grown on double-side-polished GGG substrates via LPE. The Py films ($t_{\text{Py}} = 10\text{-nm}$ and 30-nm) were subsequently deposited on the YIG films using magnetron sputtering. To ensure the strong coupling, we used in situ Ar gas rf-bias cleaning for 3 mins, to clean the YIG surface before depositing the Py layer. Reference samples of GGG/YIG/SiO₂(3-nm)/Py(10-nm), GGG/YIG/Cu(3-nm)/Py(10-nm) were also prepared at the same growth condition.

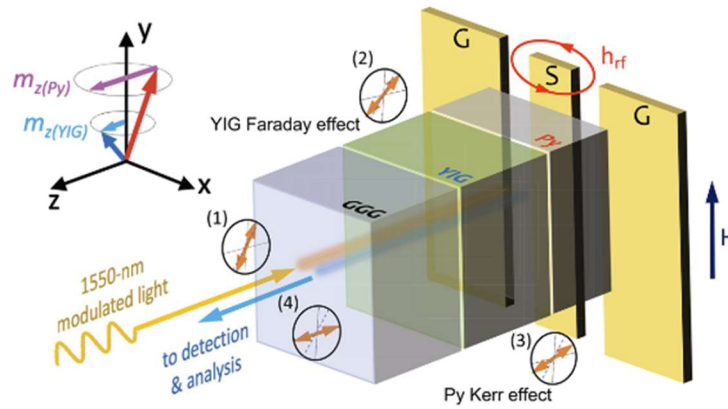


Figure 29. Schematic illustration of the experimental setup. Modulated and linearly-polarized 1550-nm light enter the sample at a polarization angle (1); dynamic Faraday effect of the YIG causes the polarization to rotate (2); dynamic Kerr effect of the Py causes polarization to further rotate (3); the reflected light, upon the returning path, picks up again the Faraday effect and causes the polarization to further rotate (4), before entering light detection and analysis. The applied dc magnetic field is parallel to the ground-signal-ground (G-S-G) lines of the CPW.

Figure 29 illustrates the measurement configuration. The modulated and linearly-polarized 1550-nm light passes through the transparent GGG substrates and detects the dynamics Faraday and Kerr signals upon their FMR excitation. As the light travels through the YIG bulk, the dynamic Faraday rotation due to the YIG FMR is picked up. Similarly, the dynamic Kerr rotation caused by the Py FMR is then picked up when the light reaches the Py layer. The Py layer also serves as a mirror and reflects the laser light. Upon reflection, the dynamic Faraday effect from the YIG is picked up again, making the effective YIG thickness $6\text{-}\mu\text{m}$, i.e., twice the film thickness. It should be noted that the Faraday rotations for the incoming and returning light add up as opposed to cancel, due to the inversion of both the chirality of the Faraday rotation and the projection of the perpendicular magnetization of YIG along the wavenumber direction, whose mechanism is akin to a commercial “Faraday rotator” often encountered in fiber optics.

The YIG/Py samples are chip-flipped on a CPW for microwave excitation and optical detection, as depicted in *Figure 29*. An in-plane magnetic field, H , along the y -direction saturates both the YIG and Py magnetizations. We scanned the frequency (from 4 to 8 GHz) and the magnetic field, and then measured the optical responses using a lock-in amplifier’s in-phase X ($\text{Re}[V_o]$) and quadrature Y ($\text{Im}[V_o]$) channels as well as the microwave transmission using a microwave diode.

4.2 Results and Discussion

Figure 30 compares the optical rectification signals between the 10-nm-Py sample and the YIG/SiO₂/Py reference sample measured at 5.85 GHz. The 10-nm-Py sample (solid line) shows the representative features of the detected FMR and hybridized PSSW modes.

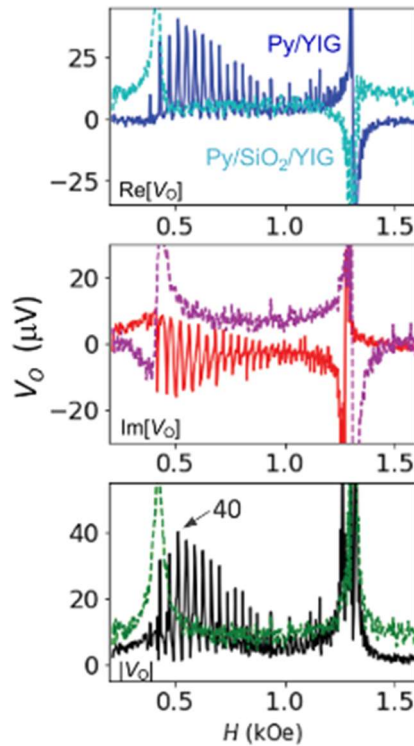


Figure 30. Example signal trace for YIG/Py (solid) and YIG/SiO₂/Py (dashed) measured at 5.85 GHz, showing the in-phase X (top) and quadrature Y (middle), and the total amplitude, $\sqrt{X^2 + Y^2}$ (bottom).

The complete fine-scan lineshape and dispersion data for the 10-nm-Py sample are summarized in *Figure 32*. A total of more than 40 PSSW modes can be identified in a broad range of frequencies. The frequency step used in the fine scan is 0.01 GHz. By

comparing the total optical signal, V_o in *Figure 32 (c)*, with the simultaneous electrical diode signal, V_{diode} in *Figure 32 (d)*, we found that more PSSW modes can be identified from the optical dataset than the electrical counterpart. In addition, the optical dataset has a much less noisy background. Such a direction comparison further shows the advantages of using magneto-optical effects for the present and relevant studies.

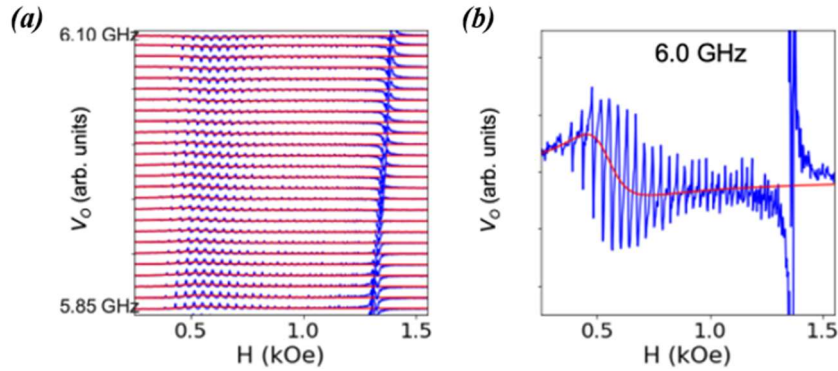


Figure 31. (a) Lorentzian fits for the $\text{Re}[V_o]$ dataset of the 10-nm-Py sample at the same frequency window. The fitting allows the subtraction of the global Py-FMR envelope and then exposure of the YIG-PSSW series. (b) A zoom-in example of the raw signal trace and fitting curve for Py-FMR at 6 GHz.

To expose the pure YIG-PSSW lineshapes, we subtract, via Lorentzian fits, the Py-FMR profile from the raw signal traces, $\text{Re}[V_o]$. *Figure 31 (a)* shows the waterfall plot of the Lorentzian fits for the $\text{Re}[V_o]$ dataset of the 10-nm-Py sample at the same frequency window as in *Figure 39*. The pure YIG-PSSW series after this Py-FMR subtraction is in *Figure 40*.

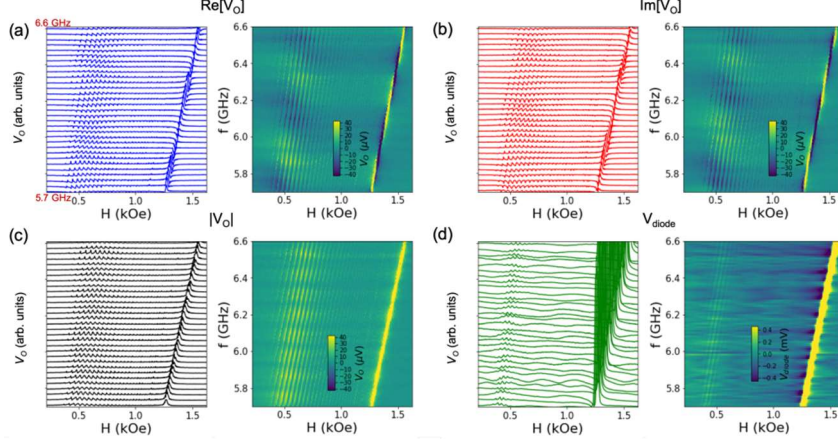


Figure 32. Dataset for the 10-nm-Py sample. The optically detected (a) in-phase, $\text{Re}[V_o]$, (b) quadrature, $\text{Im}[V_o]$, (c) total optical signal, V_o , and (d) microwave diode signal, V_{diode} , as a function of the magnetic field and frequency (5.7 ~ 6.6 GHz).

The optical signals with the phase information are obtained by the lock-in's in-phase X ($\text{Re}[V_o]$, top panel) and quadrature Y ($\text{Im}[V_o]$, middle panel), which are further used to calculate the total amplitude, $\sqrt{X^2 + Y^2}$, (bottom panel).

The YIG FMR signal at ~ 1.3 kOe is accumulated from the Faraday effect corresponding to the spatially uniform precession of the YIG magnetization. The FMR dispersion is described by the Kittel formula: $\omega^2/\gamma^2 = H_{\text{FMR}}(H_{\text{FMR}} + M_s)$, where ω is the mode frequency, $\gamma/2\pi = (g_{\text{eff}}/2) \times 28$ GHz/T is the gyromagnetic ratio, g_{eff} is the g-factor, H_{FMR} is the resonance field, and M_s is the magnetization. The excitation of the YIG PSSW modes introduces an additional exchange field H_{ex} to the Kittel equation, as $\mu_0 H_{\text{ex}} = (2A_{\text{ex}}/M_s)(n\pi/d_{\text{YIG}})^2$, which defines the mode splitting between the PSSW modes and the

uniform mode. Here A_{ex} is the exchange stiffness, and d_{YIG} is the YIG film thickness. A total of more than 30 PSSW modes can be identified for the 10-nm-Py sample.

The Py FMR at ~ 0.6 kOe is strongly modulated by the YIG PSSW modes, exhibiting the MIT effect, due to the formation of hybrid magnon modes. Besides, the YIG PSSW signals near the Py FMR regime ($n > 25$) are much stronger than the off-resonance regime ($n < 25$), which indicates the important role of the Py/YIG coupling in exciting the relevant PSSW modes and resonantly enhancing the magnetization dynamics. As a comparison, no apparent PSSW modes are observed for the Py/SiO₂/YIG reference sample, in *Figure 30* (dashed line), indicating that only the Py but not the YIG PSSWs couples to the microwave drive in the MIT regime. The Py resonance linewidth also is much narrower.

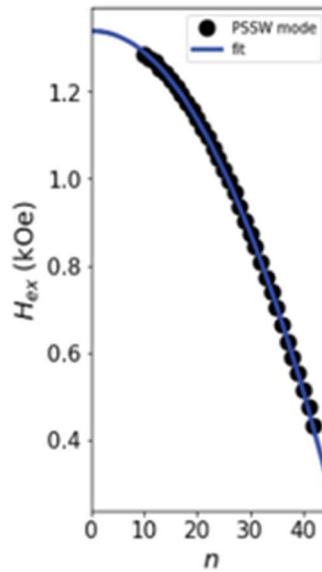


Figure 33. Plotting and the fitting of the observed PSSW modes versus the resonance fields.

In *Figure 33*, the quadratic increase of Hex with the mode number n confirms the observation of the PSSWs. Fittings to the Kittel equation and the exchange field expression yield $M_s = 1.97$ kOe and $A_{ex} = 3.76$ pJ/m, which are in good agreement with the previously report values^[179-182]. *Figure 34* plots the theoretically predicated MIT effect showing the lineshape of the Py FMR mode that is coupled to the YIG PSSW modes. The center curve with a zero-resonance detuning is a characteristic of the MIT effect. The magnon-magnon coupling induces a set of sharp dips in the spectra. Such dips in the optical reflection means a peak in their transmission, which is referred to as a transparency window in quantum optics, resembling the EIT phenomenon in photonics^[184] and optomechanics^[174, 185].

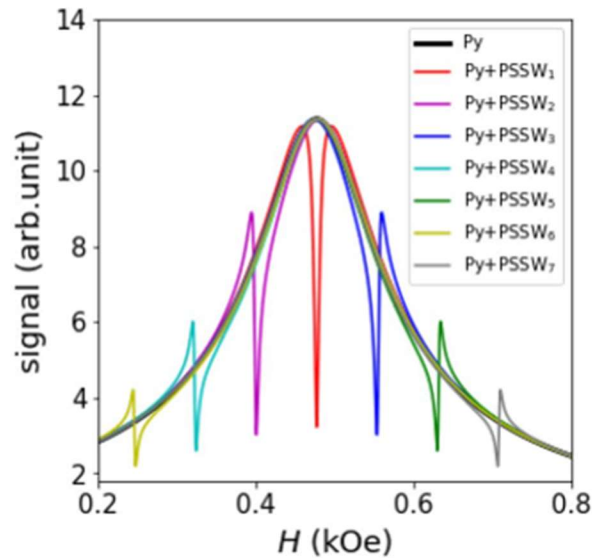


Figure 34. Theoretical signal trace of the MIT effect of the YIG/Py bilayer, 7 hybrid PSSW modes are shown as an example.

The YIG/Py interfacial exchange coupling can be also found from the H_{FMR}^{Py} shift comparing to the YIG/SiO₂/Py reference sample. As shown in *Figure 30*, the Py resonance occurs at a higher field when Py is in direct contact with YIG due to the interfacial exchange coupling. The increase of H_{FMR}^{Py} suggests that the YIG/Py interface induces a negative effective field onto Py. We found a resonance offset of $H_{FMR,offset}^{Py} = 0.17$ -kOe from *Figure 30*, which further yields a fieldlike coupling strength from the interfacial exchange, $g = H_{FMR,offset}^{Py} \times 0.9 \sqrt{M_{Py} t_{Py} / M_{YIG} t_{YIG}}$. Taking $M_{YIG} = 1.97$ -kOe, $M_{Py} = 10$ -kOe, $t_{Py} = 10$ -nm, and $t_{YIG} = 3$ - μ m.

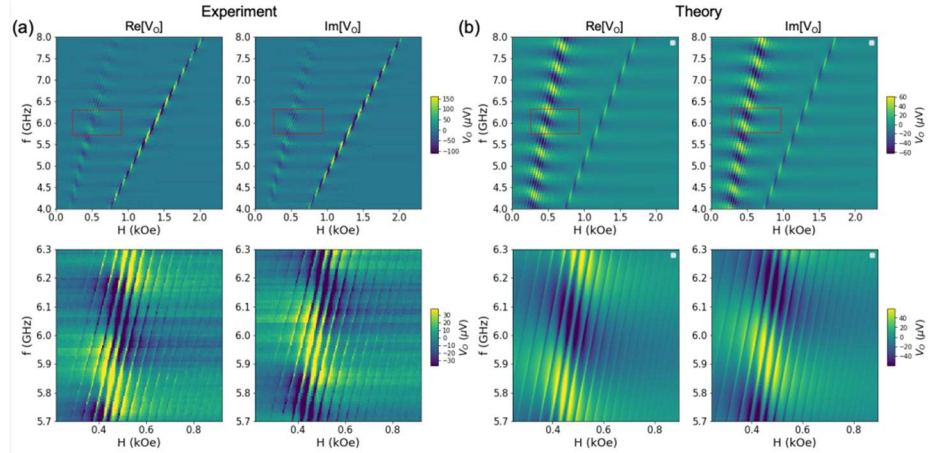


Figure 35. Dataset for the 30-nm-Py sample. (a) The optically detected in-phase, $\text{Re}[V_0]$, and quadrature, $\text{Im}[V_0]$ for the 30-nm-Py sample as a function of the magnetic field and frequency, showing the frequency-dependent phase evolution. (b) Theoretical modeling of the experimental data in (a) using the extracted fitting parameters. The bottom panels are the fine-scans at smaller field and frequency steps corresponding to the boxes in the top panel (5.7 ~ 6.3 GHz).

The full- and find-scan dispersion data, as well as the corresponding theoretical modeling data, for the 30-nm-Py sample are summarized in *Figure 35*, showing the respective in-phase, $\text{Re}[V_o]$, and quadrature, $\text{Im}[V_o]$ signals. Clear phase evolution can be observed in the optical signals $\text{Re}[V_o]$ and $\text{Im}[V_o]$. The periods of the phase evolution are the same for both YIG and Py lines, due to the fixed path difference of the measurement geometry, i.e., $\phi_L - \phi_{MW} - \phi_h$. The Py and YIG FMR lines also exhibit a small, but fixed phase offset, which could be due to either the intrinsic phase buildup from the Py-Kerr and YIG-Faraday effects, or a phase lag of the Py FMR with respect to the YIG FMR, caused by the coupled PSSW's "dragging" the hybrid YIG-Py resonances, i.e., from a finite $\phi_{\chi(\text{Py})} - \phi_{\chi(\text{YIG})}$. It is noted that this effect is unlikely due to the additional travelling distance inside the 3- μm YIG bulk, as this thickness is too small compared with the microwave wavelength.

Figure 36 compare the experimental and theoretical spin-wave dispersion using the total amplitude signal $\sqrt{X^2 + Y^2}$, whilst the individual channels, X and Y , as well as the corresponding theoretical plots.

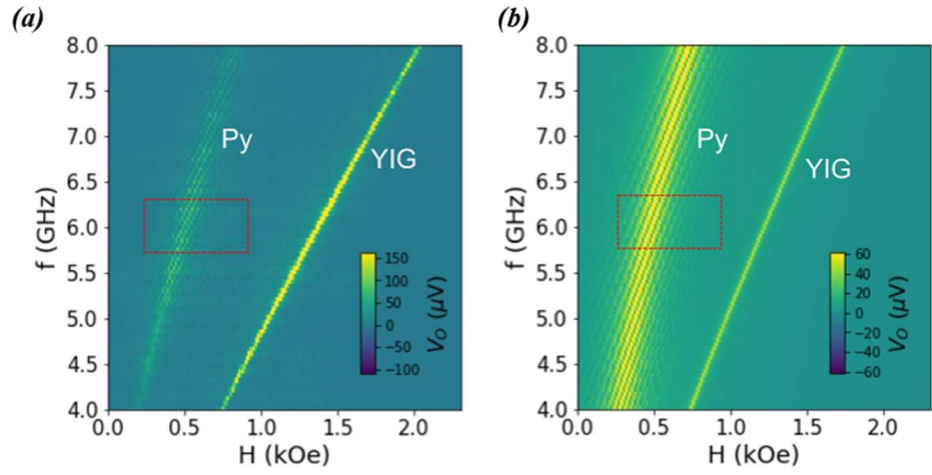


Figure 36. (a). Full scan of the signals, $|V_o|$, as a function of the magnetic field and frequency. (b). Theoretical calculated dispersion using the fitting parameters, reproducing the experimental data in (a).

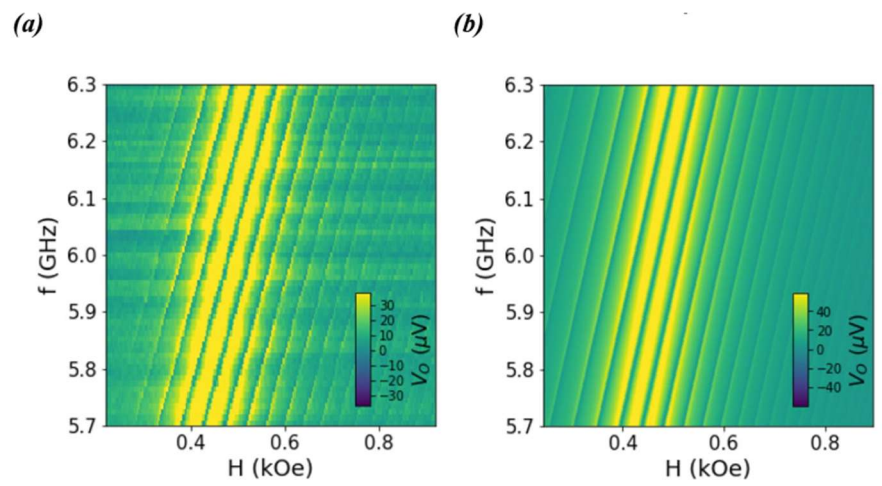


Figure 37. Fine-scans at smaller field and frequency steps corresponding to the boxes in Figure 36 (5.7 ~ 6.3 GHz).

To better analyze the hybrid PSSW modes, we show the zoom-in scan between 5.7 and 6.3 GHz and 0.2 to 0.9 kOe in *Figure 37*, which covers the Kittel dispersion of the Py. We clearly identify the distinct PSSW modes strongly “chopping” the Py FMR line. In particular, the Py resonance is attenuated to nearly the background level (non-absorption condition) at the PSSW resonance dips.

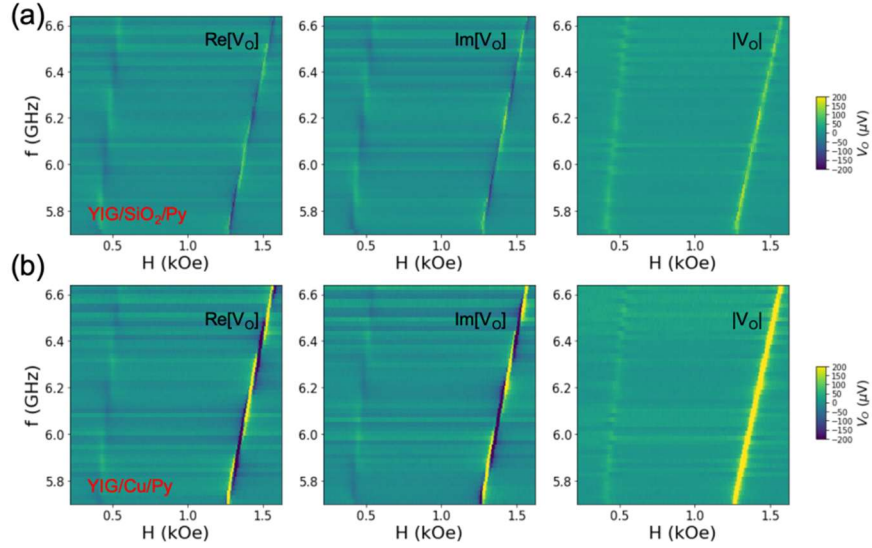


Figure 38. Dataset for the reference samples. The optically detected in-phase, $\text{Re}[V_o]$, quadrature, $\text{Im}[V_o]$, and the amplitude, V_o , for (a) YIG/SiO₂(3-nm)/Py (10-nm) and (b) YIG/Cu (3-nm)/Py (10-nm) reference samples as a function of the magnetic field and frequency.

The same measurements are also performed for the reference samples, YIG/SiO₂/Py and YIG/Cu/Py. The fine-scan optical signals, $\text{Re}[V_o]$, $\text{Im}[V_o]$, and the total amplitude for the reference samples as a function of the magnetic field and frequency, as shown in *Figure 38*. No YIG PSSWs are observed in the YIG/SiO₂/Py and YIG/Cu/Py references, suggesting that the coupling is through the exchange interaction at the

interface as opposed to the dipolar interaction. In addition, the Py Kerr signal is attenuated in the Py/Cu/YIG as compared to Py/SiO₂/YIG, which is likely due to the metal refractive index of the inserted Cu layer.

To further examine the detuning range and its characteristics, we separate the Py resonance envelope with the YIG PSSW modes. Such analysis can be made via fitting either the raw $\text{Re}[V_o]$ or $\text{Im}[V_o]$ data. *Figure 39* shows the raw $\text{Re}[V_o]$ signal of the hybrid modes at a representative frequency window (5.85 ~ 6.1 GHz) for the 10-nm-Py sample.

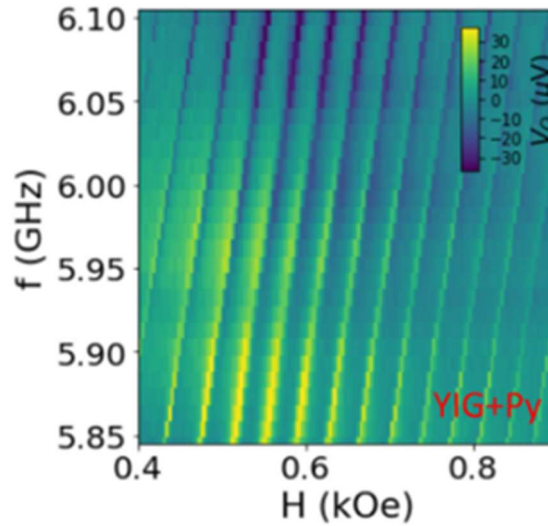


Figure 39. The $\text{Re}[V_o]$ signal at a representative frequency window (5.85 ~ 6.1 GHz) for the 10-nm-Py sample.

After subtracting the Py resonance profile, we can fit each PSSW series (labeled $n = 32 \sim 43$) to a phased-shifted Lorentzian function yielding the resonance and linewidth for each PSSWs, as shown in *Figure 40* (where the highlighted section shows an example series at $n = 39$).

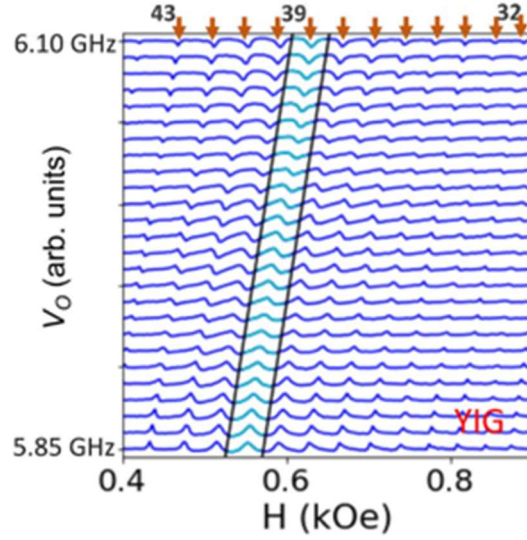


Figure 40. YIG PSSW lineshape (12 modes series near the Py resonance are labeled and analyzed, $n = 32 \sim 43$) after subtracting the Py resonance profile. The highlighted section is an example series at $n = 39$.

Figure 41 (a) shows the resonance field H_{PSSW}^{YIG} of the PSSW series (thin lines, from $n = 32 \sim 43$) comparing to the H_{PSSW}^{Py} (single thick line). The shaded area indicates the Py linewidth, which is centered at the H_{PSSW}^{Py} and is also much enhanced as compared to the case without the mode coupling (in the YIG/SiO₂/Py sample). Next, we plot the ΔH_{res} at each frequency and for all the PSSW series with the corresponding YIG PSSW linewidth, ΔH_{YIG} , in Figure 41 (b).

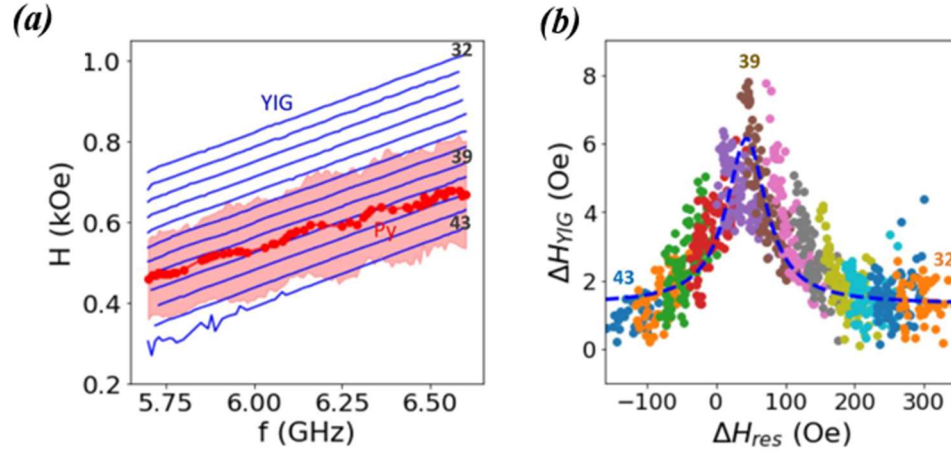


Figure 41. (a) Resonance field, H_{PSSW}^{YIG} of the PSSW series and the H_{FMR}^{Py} envelope. The shaded area reflects the Py linewidth. (b) The extracted YIG PSSW linewidth ΔH_{YIG} versus the ΔH_{res} at each frequency and for all the PSSW series.

We clearly observed a modulation effect of the YIG linewidth, ΔH_{YIG} , from ~ 2 Oe to ~ 10 Oe, spanning across the magnon-magnon coupling regime. This observation provides strong evidence that the MIT linewidth is broadened due to the additional energy dissipation by coupling the YIG PSSW modes to the Py FMR mode, also known as the Purcell regime.

CHAPTER FIVE

STUDY ON MAGNETOELECTRIC EFFECT ON HEXAGONAL FERRITE MATERIAL $\text{Ba}_2\text{Zn}_2\text{Fe}_{12}\text{O}_{22}$ (Zn_2Y) FOR APPLICATION OF ELECTRIC FIELD TUNABLE RESONATORS

Resonators, filters, and other frequency-selective components are essential parts of RF and microwave systems, including communication systems, radars, measuring equipment, etc. These components are employed to alternatively filter or suppress a certain region of the passing signal's frequency spectrum and modify it in accordance with the intended pattern. In particular, bandpass filters are used to selectively transmit signals with reasonably low loss and suppress signals outside the band. The filter bandwidth requirements vary depending on the application; for example, a pre-selector in a spectrum analyzer may need a very small span, but an ultra-wideband communication system may require components with a large bandwidth. Getting the system above reconfigurable, which will entail the construction of tunable subcomponents, is one particular way to increase performance and capabilities.

Dielectric resonators with semiconductor or ferroelectric materials, printed circuit boards with varactors, pin diodes or MEMs, cavity filters with adjustable gaps, etc. have all been used to create electronically controlled transfer functions. Filters based on spin-wave excitations have among other technologies demonstrated a potential for developing tiny, planar, and tunable components. Because they use low-loss ferrites, their microwave

characteristics can be adjusted across a large frequency range using a source of changeable external magnetic field. These filters also exhibit substantially nonreciprocal properties in some configurations, combining the characteristics of filters and isolators. Despite these benefits, the requirements for a source of a variable magnetic field poses several difficulties in terms of device size, weight, and power consumptions. Due to this, attempts have been made to create ferrite-base components that have different methods for frequency tuning. Recent studies in this field include adjusting the dielectric constant in ferrite-ferroelectric composites and modifying the electric field of resonators and filters via strain-mediated coupling in ferrite-piezoelectric composites.

ME multiferroics, which combine coupled electric and magnetic dipoles, have a great deal of potential for use in future electronics systems. It has been demonstrated that intricate internal arrangements of magnetic moments can cause ferroelectricity. When an external magnetic field is applied, magnetically induced ferroelectrics are known to exhibit gigantic ME effects, or changes in ferroelectric polarization. However, it typically occurs at temperatures that are too low and with applied high enough magnetic field to be effective. As a result, one of the biggest challenges in ME research is identifying a strong room-temperature ME effect.

The future development of low-power spintronics must focus on the control of magnetism by electric fields. We will be able to combine the benefits of magnetic components with the potential for fast, low-cost, and energy-efficient electric tuning, in particular, thanks to the realization of such controls. Purely electronic or electrostatic effects

or strain coupling can both cause the electric field influence on magnetism. Such direct electric field modification of magnetic order parameters is possible in multiferroic materials^[186-188]. Due to either a specific crystallo-magnetic structure or specific types of non-collinear magnetic properties is made possible in single-phase materials, composites with ferroelectric or semiconductors, and in composites with ferroelectrics and semiconductors. This research involves a Y-type hexagonal ferrite filter that is dual magnetic field and electric field tunable. With the aid of an integrated permanent magnet, the filter's magnetic field, H , can be tuned, and the electric field, E , tuning was made possible by the recently discovered nonlinear magnetoelectric (NLME) phenomenon in M- and Y-type hexagonal ferrites. The magnetization and magnetocrystalline anisotropy fields of ferrite were observed to vary when a pulsed current or DC electric field was applied, and the changes in the order parameters were proportional to E^2 . The FMR frequency was tuned as a result of these changes in the magnetic parameters, and the frequency variations were proportional to the DC electric power delivered to the sample, as a coupling component, hexagonal ferrite is used. Thus, the electric field or current tunability was achieved by using hexagonal ferrite as the coupling element. We will go through the material's magnetic and electric field tuning properties in the sections that follow.

5.1 Experimental Setup

Here, a thick platelet of a Y-type hexaferrites, $\text{Ba}_2\text{Zn}_2\text{Fe}_{12}\text{O}_{22}$ (Zn_2Y), is suitable for dual magnetic and electric field tunable devices. This sample used in this work was

prepared by LPE (provided by Prof. Srinivasan, Department of Physics, Oakland University). The schematic of the filter are shown in *Figure 42*. A microstrip line with 50 Ohm impedance manufactured using 0.01-inch-thick RT/Duroid 5880 and the ferrite, Zn_2Y , was positioned on top of the stripline and oriented with longer side along the microstrip. Two platinum electrodes were deposited at opposite edges of the sample, allowing the application of a voltage to establish an electric field parallel to the sample plane. Thus, the resulting flow of a DC electric current through the ferrite is the basal plane. A thin 15- μm sheet of isolating material (mica) was placed between the sample and the microstrip line to avoid electrical contact.

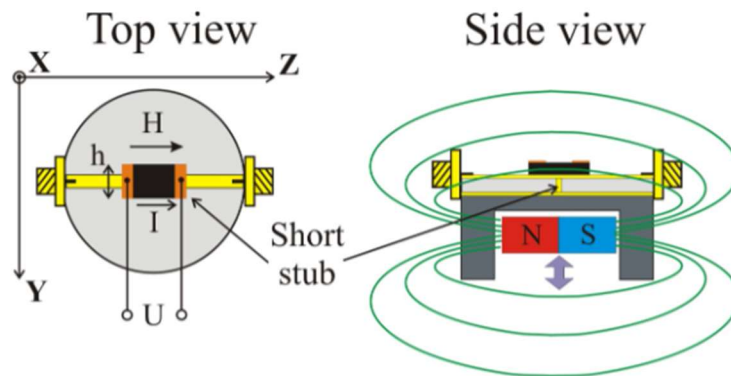


Figure 42. Schematics of the ferrite-based band-pass filter prototype showing the position of Zn_2Y magnetostatic resonator atop of the short-circuited microstrip line and bias permanent magnet inside the filter's frame.

A disk-shaped permanent magnet as shown in *Figure 42* was used to generate the necessary bias magnetic field, H_0 , parallel to the sample plane as indicated by the magnetic field lines. The field H_0 was found to be uniform over the entire volume of the ferrite and the field strength could be varied by adjusting the separation between the magnet

and the device ground plane. When the ferrite is magnetized to saturation, it is able to support multiple magnetostatic wave (MSW) modes, with the resonance frequencies depending on H_0 , saturation magnetization, and the anisotropy field values. The crystallographic c-axis was oriented perpendicularly to the sample. The easy plane for magnetization coincided with the sample plane. The sample was subjected to an in-plane electric field E when a voltage was applied between the electrodes, resulting in a DC current in the easy plane.

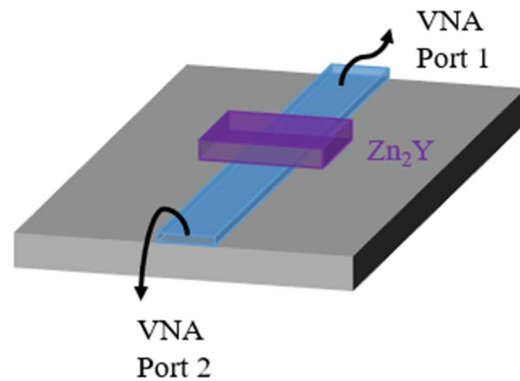


Figure 43. Schematics of the FMR measurement of the ferrite material, Zn_2Y , on top of a microstrip transmission line with a series of bias external magnetic fields

Usually, FMR in a sample is excited by placing the sample in a uniform microwave magnetic field. An onset of FMR is easily seen as applied-field dependent resonance absorption of the microwave power by the magnetic material. To excite FMR in ferro- and ferrimagnetic films is by placing them on top of a microstrip or coplanar microwave stripline transmission line or forming a microstrip line directly on top of the film. A static magnetic field H is applied in the plane of the film in the direction

perpendicular to the microstrip line. A microwave current flowing through the microstrip feeding line excites a photon resonance in the SRR. In the resonance, a significant microwave current flows through the SRR. Its Oersted field drives magnetization precession in the Zn_2Y film.

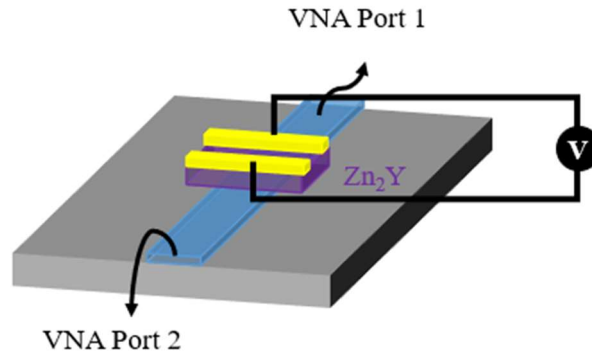


Figure 44. Schematics of the small DC voltage applied to the ferrite material, Zn_2Y , which mounts on top of the transmission line.

In order to take the measurements in the frequency domain, the input, and the output of the microstrip feeding line have been connected to the ports of a VNA and its transmission characteristics, $S_{21} = \text{Re}[S_{21}] + i\text{Im}[S_{21}]$ has been measured as a function of microwave frequency f and the strength H of the applied field.

5.2 Results and Discussion

Since the ferrite slab is tangentially magnetized, it can support two types of magnetostatic waves, namely magnetostatic surface waves (MSSW) and backward volume waves (MSBVW). The former is known to propagate in the direction perpendicular to

bias magnetic field whereas the latter propagation is parallel to the bias magnetic field. In our research, the corresponding S-parameters were measured with a vector network analyzer (Agilent PNA N5230A). The magnitudes of the scattering matrix parameters $|S_{21}|$ and $|S_{12}|$, as well as reflection coefficient S_{11} , were measured under a series of bias magnetic fields. Representative data shown in *Figure 45*.

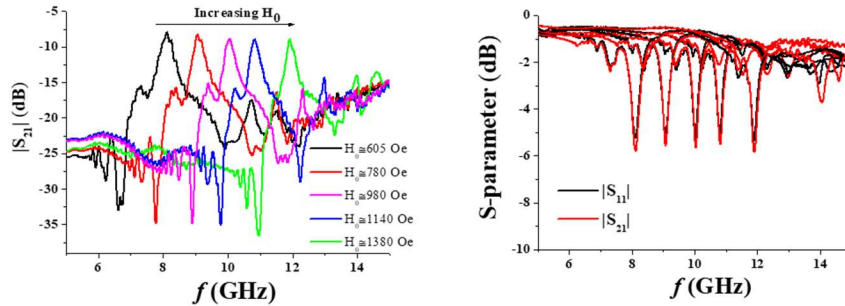


Figure 45. The measured transmission characteristics (a) and reflection coefficient (b) of the bandpass filter under different bias fields.

During these measurements, no DC voltage was applied to the sample. The actual values of the bias field H_0 were not recorded due to the magnetic field was produced by a permanent magnet and thus was spatially non-uniform. When the bias magnetic field is measured outside the sample, the difference between the value registered by the Gaussmeter and the actual field at the position of ferrite resonator would be very different for any meaningful comparison.

Figure 46 provides the data on the relation between resonance frequency and bias field for a Zn_2Y platelet that was placed in a uniform magnetic field produced by an

electromagnet. Specifically, the resonance frequency ranges from 8 GHz to 12 GHz for the bias field interval of 550 Oe ~ 1400 Oe.

Figure 46 shows profiles of $|S_{21}|$ and $|S_{12}|$ versus frequency and the band-pass characteristic of the filter shows slight nonreciprocity that could be attributed to a non-symmetrical position of the resonator with respect to the short-circuit metal slab, and thus to non-equal coupling of the resonator modes with the electromagnetic signals coming from the two opposite directions.

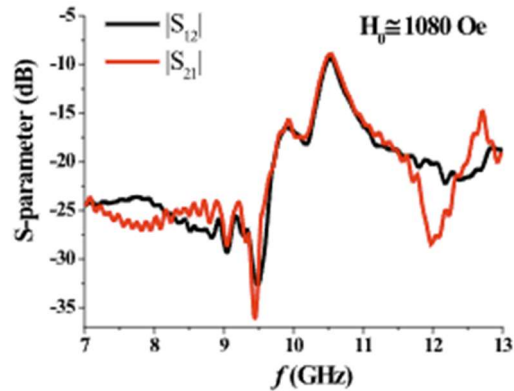


Figure 46. Comparison between the measured filter’s characteristics for the opposite directions of the signal propagation.

The insertion loss and 3-dB bandwidth of the filter measured with the change of the center frequency of the filter are plotted in the *Figure 47*. One notices that within the X-band, the insertion loss is in the 8-9 dB range. From the reflections coefficients shown in *Figure 45*, one may attribute such losses, in part, to the poor matching between the resonator and both input and output transmission lines.

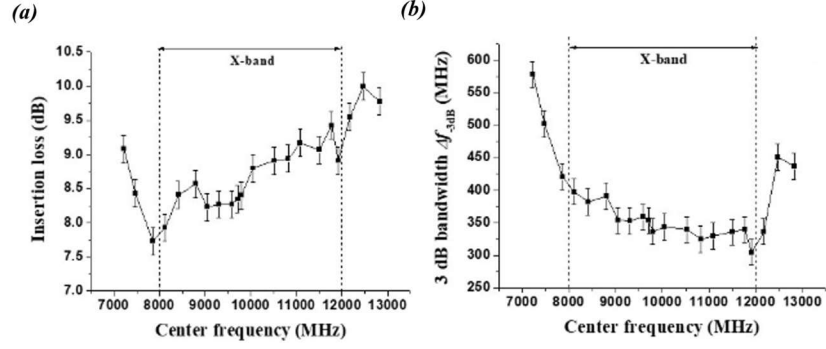


Figure 47. Band-pass filter performance throughout the X-band: (a) insertion loss, (b) 3-dB bandwidth

A capacitive matching circuit on both sides of the ferrite sample might reduce the insertion loss. The filter bandwidth is rather large in comparison, for example, with YIG filters. The contributing factor, besides bias field nonuniformity, is the large losses in Zn_2Y . The full 3-dB linewidth of the two-side coupled resonator is given by

$$\Delta f_{-3dB} = f_c \frac{(1 + K_1 + K_2)}{Q_0}$$

where f_c is the center frequency, $K_l > 0$ are the coupling coefficients with the input and output transmission lines, and Q_0 is the unloaded quality factor that accounts for internal losses in resonator. In turn, Q_0 is determined by the internal magnetic field and the FMR linewidth. For in plane magnetized film $Q_0 = H_0/\Delta H$. Therefore, for the comparable values of f_c and resonator made with smaller ΔH material will have a proportionally narrower linewidth. Since the lowest ΔH values for single-crystal Zn_2Y are on the order of 10^{-15} Oe whereas the best YIG films have $\Delta H \sim 1$ Oe, it is not surprising that the

narrowest 3 dB linewidths of 10 ~ 20 MHz for YIG-based filters will be unattainable for Zn_2Y filters.

The dual tunability of the bandpass filter was demonstrated by applying a DC current along the sample basal plane and recording the ME effect induced changes in the transmission characteristics. The small-signal resistance of the sample was $R = 6.7 \text{ k}\Omega$ at room temperature. Due to semiconductor nature of the ferrite material, the linear dependence between applied voltage U and current I maintained only in a limited range of I and voltage-current characteristic reached saturation for $I > 10 \text{ mA}$. This sets the limit for the maximum applied current. Representative profiles for tuning the pass band by applied DC currents are presented in *Figure 48 (a)*. One notices a noticeable downshift of the center frequency due to the current. This is expected based on results of our studies in hexagonal ferrites that showed a decrease in the effective magnetization $4\pi M_{eff}$ leading to a decrease in the mode frequency. The measured center frequency dependence on applied input power $P = UI$ for difference bias magnetic fields are shown in *Figure 48 (b)*. A current-tunable center frequency shift of more than 1 GHz is routinely obtained for applied power $P \approx 200 \text{ mW}$. The absolute frequency shift is larger for the frequencies around 12 GHz in comparisons with frequencies close to 8 GHz. Larger frequencies mean larger applied magnetic field H_0 which, being a prefactor for $4\pi M_{eff}$, enhances its effect.

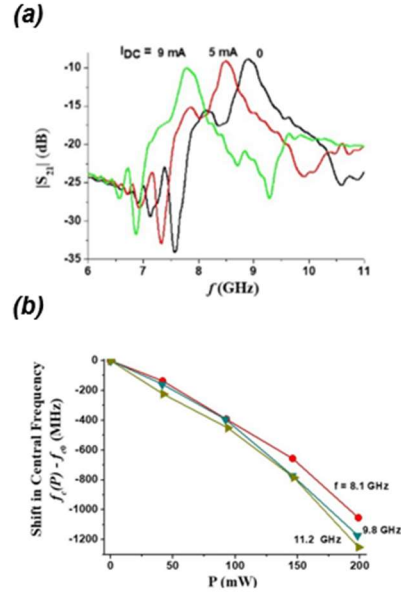


Figure 48. (a) Characteristics tuning by applied DC current due to the nonlinear ME effect. (b) Center frequency dependence on the applied electric power.

Finally, it is seen that for relatively small currents, the filter mostly retains the insertion loss and bandwidth values, whereas for large current, both parameters deteriorate. This may be due to the changes of complex microwave impedance of ferrite materials which are known to take place in semiconductors with the increase of applied constant voltage. The impedance changes will affect matching conditions and increased internal losses will decrease the unloaded Q -factor.

CHAPTER SIX

SUMMARY AND FUTURE WORK

This dissertation focused on my research effort in developing a novel detection method for magnon-magnon coupling in exchange coupled YIG/Py bilayers with magneto-optical effects and investigating the possibility of control of magnetization dynamics by using voltage-driven electric field. These findings are essential for miniaturizing the size of semiconductors and achieving better performance by consuming less power than conventional electronics.

The observation of the magnetically-induced transparency in YIG/Py bilayers exhibiting magnon-magnon coupling. The use of the thin-film YIG system shows great potential in practical applications. The series of standing waves in YIG may allow to build an evenly distributed resonance array in a single YIG device, which may lead to relevant applications such as memory and comb generation^[189-191]. In addition, compared with the so-far widely used hybrid magnonic systems that utilize the ferromagnetic resonances, our results pave the way towards building more complex hybrid systems with spin-waves. Our measurement is achieved via a simultaneous and stroboscopic detection of the coupled magnetization dynamics using a single wavelength, therefore avoids the possible artifacts due to multiple probes. Our work, performed in a planar structure as opposed to 3D cavities, also paves the way towards solving strong magnon-magnon

couplings by the state-of-the-art spin-orbitronic toolkits^[192, 193], involving emerging materials such as antiferromagnets^[194-196], 2D monolayers^[197-200], and topological insulators^[201, 202].

We also reported that the electric field/current-induced ME effect in a hexaferrite material, Zn_2Y . Single crystal thin films made by LPE were used for studies on ME effect and the key advantage for use of the ferrite materials in the high frequency devices is that the magnetic properties can be tuned by both magnetic and electric field. The ME coefficient was determined from the shift in the resonance frequency and the estimated variations in the magnetic parameters.

The tuning characteristics may be significantly impacted by the Joule heat produced in the hexagonal ferrite film, Zn_2Y , when the tuning electric current I is high. As a result, this research can be looked at further. We will first characterize the temperature dependence of the tuned frequency shift in order to decouple the thermal effect on the magnetic responses and electric field tunability of the devices. The objective is to monitor the ferromagnetic layer of the device's magnetic responses at various temperatures. To facilitate quick but precise device characterizations, we will prepare a small-sized testbed with well controlled temperature range and stability. A Peltier cooling device with a pulse width modulation temperature control system will be used in the characterization owing to the size of the miniaturized device. For the closed-loop control system, a precise temperature sensor will be positioned close to the surface of the device being tested.

REFERENCES

1. Verschuur, G.L., *Hidden attraction: the history and mystery of magnetism*. 1996: Oxford University Press.
2. Griffiths, J.H., *Anomalous high-frequency resistance of ferromagnetic metals*. Nature, 1946. **158**(4019): p. 670-671.
3. Kruglyak, V., S. Demokritov, and D. Grundler, *Magnonics*. Journal of Physics D: Applied Physics, 2010. **43**(26): p. 264001.
4. Khitun, A., M. Bao, and K.L. Wang, *Magnonic logic circuits*. Journal of Physics D: Applied Physics, 2010. **43**(26): p. 264005.
5. Lenk, B., et al., *The building blocks of magnonics*. Physics Reports, 2011. **507**(4-5): p. 107-136.
6. Chumak, A.V., et al., *Magnon spintronics*. Nature Physics, 2015. **11**(6): p. 453-461.
7. Csaba, G., Á. Papp, and W. Porod, *Perspectives of using spin waves for computing and signal processing*. Physics Letters A, 2017. **381**(17): p. 1471-1476.
8. Kajiwara, Y., et al., *Transmission of electrical signals by spin-wave interconversion in a magnetic insulator*. Nature, 2010. **464**(7286): p. 262-266.
9. Wang, Z.K., et al., *Observation of frequency band gaps in a one-dimensional nanostructured magnonic crystal*. Applied Physics Letters, 2009. **94**(8): p. 083112.
10. Yu, H., et al., *Approaching soft X-ray wavelengths in nanomagnet-based microwave technology*. Nature Communications, 2016. **7**(1): p. 11255.
11. Schneider, T., et al., *Realization of spin-wave logic gates*. Applied Physics Letters, 2008. **92**(2): p. 022505.
12. Demokritov, S.O., et al., *Tunneling of Dipolar Spin Waves through a Region of Inhomogeneous Magnetic Field*. Physical Review Letters, 2004. **93**(4).

13. Seo, S.-M., et al., *Current-Induced Control of Spin-Wave Attenuation*. Physical Review Letters, 2009. **102**(14).
14. Wang, Z., et al., *Control of Spin Waves in a Thin Film Ferromagnetic Insulator through Interfacial Spin Scattering*. Physical Review Letters, 2011. **107**(14).
15. Hamadeh, A., et al., *Full Control of the Spin-Wave Damping in a Magnetic Insulator Using Spin-Orbit Torque*. Physical Review Letters, 2014. **113**(19).
16. Vlaminck, V. and M. Bailleul, *Current-induced spin-wave Doppler shift*. Science, 2008. **322**(5900): p. 410-413.
17. Wolf, S., et al., *Spintronics: a spin-based electronics vision for the future*. science, 2001. **294**(5546): p. 1488-1495.
18. Žutić, I., J. Fabian, and S. Das Sarma, *Spintronics: Fundamentals and applications*. Reviews of Modern Physics, 2004. **76**(2): p. 323-410.
19. Shen, X., et al., *Spin transport properties of 3d transition metal(ii) phthalocyanines in contact with single-walled carbon nanotube electrodes*. Physical Chemistry Chemical Physics, 2010. **12**(36): p. 10805.
20. Tsukagoshi, K., B.W. Alphenaar, and H. Ago, *Coherent transport of electron spin in a ferromagnetically contacted carbon nanotube*. Nature, 1999. **401**(6753): p. 572-574.
21. Mott, N.F., *The electrical conductivity of transition metals*. Proceedings of the Royal Society of London. Series A - Mathematical and Physical Sciences, 1936. **153**(880): p. 699-717.
22. Baibich, M.N., et al., *Giant Magnetoresistance of (001)Fe/(001)Cr Magnetic Superlattices*. Physical Review Letters, 1988. **61**(21): p. 2472-2475.
23. Binasch, G., et al., *Enhanced magnetoresistance in layered magnetic structures with antiferromagnetic interlayer exchange*. Physical Review B, 1989. **39**(7): p. 4828-4830.
24. Jedema, F.J., A.T. Filip, and B.J. Van Wees, *Electrical spin injection and accumulation at room temperature in an all-metal mesoscopic spin valve*. Nature, 2001. **410**(6826): p. 345-348.
25. Jedema, F.J., et al., *Electrical detection of spin precession in a metallic mesoscopic spin valve*. Nature, 2002. **416**(6882): p. 713-716.

26. Camley, R.E. and J. Barnaś, *Theory of giant magnetoresistance effects in magnetic layered structures with antiferromagnetic coupling*. Physical Review Letters, 1989. **63**(6): p. 664-667.
27. Prinz, G.A., *Magnetoelectronics*. science, 1998. **282**(5394): p. 1660-1663.
28. Julliere, M., *Tunneling between ferromagnetic films*. Physics letters A, 1975. **54**(3): p. 225-226.
29. Maekawa, S. and U. Gafvert, *Electron tunneling between ferromagnetic films*. IEEE Transactions on Magnetics, 1982. **18**(2): p. 707-708.
30. Moodera, J.S., et al., *Large Magnetoresistance at Room Temperature in Ferromagnetic Thin Film Tunnel Junctions*. Physical Review Letters, 1995. **74**(16): p. 3273-3276.
31. Miyazaki, T. and N. Tezuka, *Giant magnetic tunneling effect in Fe/Al₂O₃/Fe junction*. Journal of magnetism and magnetic materials, 1995. **139**(3): p. L231-L234.
32. Butler, W.H., et al., *Spin-dependent tunneling conductance of Fe|MgO*. Physical Review B, 2001. **63**(5).
33. Mathon, J. and A. Umerski, *Theory of tunneling magnetoresistance of an epitaxial Fe/MgO/Fe(001) junction*. Physical Review B, 2001. **63**(22).
34. Ikeda, S., et al., *Tunnel magnetoresistance of 604% at 300K by suppression of Ta diffusion in CoFeB /MgO / CoFeB pseudo-spin-valves annealed at high temperature*. Applied Physics Letters, 2008. **93**(8): p. 082508.
35. Jiang, L., et al., *Large Tunnel Magnetoresistance of 1056% at Room Temperature in MgO Based Double Barrier Magnetic Tunnel Junction*. Applied Physics Express, 2009. **2**: p. 083002.
36. Slonczewski, J.C., *Current-driven excitation of magnetic multilayers*. Journal of Magnetism and Magnetic Materials, 1996. **159**(1-2): p. L1-L7.
37. Berger, L., *Emission of spin waves by a magnetic multilayer traversed by a current*. Physical Review B, 1996. **54**(13): p. 9353-9358.

38. Tsoi, M., et al., *Excitation of a Magnetic Multilayer by an Electric Current*. Physical Review Letters, 1998. **80**(19): p. 4281-4284.
39. Katine, J.A., et al., *Current-Driven Magnetization Reversal and Spin-Wave Excitations in Co*. Physical Review Letters, 2000. **84**(14): p. 3149-3152.
40. Stiles, M.D. and A. Zangwill, *Anatomy of spin-transfer torque*. Physical Review B, 2002. **66**(1).
41. Ralph, D.C. and M.D. Stiles, *Spin transfer torques*. Journal of Magnetism and Magnetic Materials, 2008. **320**(7): p. 1190-1216.
42. Chappert, C., A. Fert, and F.N. Van Dau, *The emergence of spin electronics in data storage*. Nature Materials, 2007. **6**(11): p. 813-823.
43. Engel, B.N., et al., *A 4-Mb toggle MRAM based on a novel bit and switching method*. IEEE Transactions on Magnetics, 2005. **41**(1): p. 132-136.
44. Bhatti, S., et al., *Spintronics based random access memory: a review*. Materials Today, 2017. **20**(9): p. 530-548.
45. Bloch, F., *Zur theorie des ferromagnetismus*. Zeitschrift für Physik, 1930. **61**(3): p. 206-219.
46. Smiciklas, M., et al., *New Test of Local Lorentz Invariance Using aNe21–Rb–KComagnetometer*. Physical Review Letters, 2011. **107**(17).
47. Crooker, S.A., et al., *Spectroscopy of spontaneous spin noise as a probe of spin dynamics and magnetic resonance*. Nature, 2004. **431**(7004): p. 49-52.
48. Graner, B., et al., *Reduced Limit on the Permanent Electric Dipole Moment of ¹⁹⁹Hg*. Physical Review Letters, 2016. **116**(16).
49. Smith, F., *Faraday Rotation of Radio Waves from the Pulsars*. Nature, 1968. **220**(5170): p. 891-892.
50. Takano, T., et al., *Spin Squeezing of a Cold Atomic Ensemble with the Nuclear Spin of One-Half*. Physical Review Letters, 2009. **102**(3).
51. Council, G., et al., *Spin wave contributions to the high-frequency magnetic response of thin films obtained with inductive methods*. Journal of Applied Physics, 2004. **95**(10): p. 5646-5652.

52. Neudecker, I., et al., *Comparison of frequency, field, and time domain ferromagnetic resonance methods*. Journal of Magnetism and Magnetic Materials, 2006. **307**(1): p. 148-156.
53. Bilzer, C., et al., *Vector network analyzer ferromagnetic resonance of thin films on coplanar waveguides: Comparison of different evaluation methods*. Journal of Applied Physics, 2007. **101**(7): p. 074505.
54. Harward, I., et al., *A broadband ferromagnetic resonance spectrometer to measure thin films up to 70 GHz*. Review of Scientific Instruments, 2011. **82**(9): p. 095115.
55. Kennewell, K.J., et al., *Magnetization pinning at a Py/Co interface measured using broadband inductive magnetometry*. Journal of Applied Physics, 2010. **108**(7): p. 073917.
56. Tsymbal, E.Y. and I. Zutic, *Spin transport and magnetism*. 2012: CRC press.
57. Griffiths, D.J., *Introduction to electrodynamics*. 2005, American Association of Physics Teachers.
58. O'Hendley, R., *Modern magnetic materials. Principles and Applications* (Johns Wiley & Sons, Inc., 2000), 1999.
59. Cherepanov, V., I. Kolokolov, and V. L'vov, *The saga of YIG: Spectra, thermodynamics, interaction and relaxation of magnons in a complex magnet*. Physics reports, 1993. **229**(3): p. 81-144.
60. Serga, A., A. Chumak, and B. Hillebrands, *YIG magnonics*. Journal of Physics D: Applied Physics, 2010. **43**(26): p. 264002.
61. Jamali, M., et al., *Spin wave nonreciprocity for logic device applications*. Scientific Reports, 2013. **3**(1).
62. Schneider, T., et al., *Phase reciprocity of spin-wave excitation by a microstrip antenna*. Physical Review B, 2008. **77**(21).
63. Demidov, V.E., et al., *Excitation of microwaveguide modes by a stripe antenna*. Applied Physics Letters, 2009. **95**(11): p. 112509.
64. Žutić, I., J. Fabian, and S.D. Sarma, *Spintronics: Fundamentals and applications*. Reviews of modern physics, 2004. **76**(2): p. 323.

65. Awschalom, D.D. and J.M. Kikkawa, *Electron spin and optical coherence in semiconductors*. Physics Today, 1999. **52**(6): p. 33-38.
66. Bader, S.D. and S.S.P. Parkin, *Spintronics*. Annual Review of Condensed Matter Physics, 2010. **1**(1): p. 71-88.
67. Fert, A., *Nobel Lecture: Origin, development, and future of spintronics*. Reviews of Modern Physics, 2008. **80**(4): p. 1517-1530.
68. Aebischer, B. and L.M. Hilty, *The Energy Demand of ICT: A Historical Perspective and Current Methodological Challenges*. 2015, Springer International Publishing. p. 71-103.
69. Andrae, A. and T. Edler, *On Global Electricity Usage of Communication Technology: Trends to 2030*. Challenges, 2015. **6**(1): p. 117-157.
70. Jones, N., *The information factories*. Nature, 2018. **561**(7722): p. 163-6.
71. Samal, D. and P.S. Anil Kumar, *Giant magnetoresistance*. Resonance, 2008. **13**(4): p. 343-354.
72. Gregg, J., et al., *Spin electronics—a review*. Journal of Physics D: Applied Physics, 2002. **35**(18): p. R121.
73. Berger, L., *Emission of spin waves by a magnetic multilayer traversed by a current*. Physical Review B, 1996. **54**(13): p. 9353.
74. Slonczewski, J., *Excitation of spin waves by an electric current*. Journal of Magnetism and Magnetic Materials, 1999. **195**(2): p. L261-L268.
75. Katine, J., et al., *Current-driven magnetization reversal and spin-wave excitations in Co/Cu/Co pillars*. Physical review letters, 2000. **84**(14): p. 3149.
76. Tsoi, M., et al., *Generation and detection of phase-coherent current-driven magnons in magnetic multilayers*. Nature, 2000. **406**(6791): p. 46-48.
77. Kiselev, S.I., et al., *Microwave oscillations of a nanomagnet driven by a spin-polarized current*. Nature, 2003. **425**(6956): p. 380-383.
78. Krivorotov, I., et al., *Time-domain measurements of nanomagnet dynamics driven by spin-transfer torques*. Science, 2005. **307**(5707): p. 228-231.

79. Myers, E., et al., *Current-induced switching of domains in magnetic multilayer devices*. Science, 1999. **285**(5429): p. 867-870.
80. Stiles, M.D. and A. Zangwill, *Anatomy of spin-transfer torque*. Physical Review B, 2002. **66**(1): p. 014407.
81. Landau, L. and E. Lifshitz, *On the theory of the dispersion of magnetic permeability in ferromagnetic bodies*, in *Perspectives in Theoretical Physics*. 1992, Elsevier. p. 51-65.
82. Gilbert, T.L., *Classics in Magnetism A Phenomenological Theory of Damping in Ferromagnetic Materials*. IEEE Transactions on Magnetism, 2004. **40**(6): p. 3443-3449.
83. Suhl, H., *Theory of the magnetic damping constant*. IEEE Transactions on Magnetism, 1998. **34**(4): p. 1834-1838.
84. Faraday, M., *I. Experimental researches in electricity.—Nineteenth series*. Philosophical Transactions of the Royal Society of London, 1846. **136**(0): p. 1-20.
85. Landau, L.D. and E.M. Lifshitz, *Course of theoretical physics*. 2013: Elsevier.
86. Kerr, J., *XL. A new relation between electricity and light: Dielectric media birefringent*. The London, Edinburgh, and Dublin Philosophical Magazine and Journal of Science, 1875. **50**(332): p. 337-348.
87. Ando, K., *Magneto-optics (springer series in solid-state science)*. Springer, Berlin, 2000) vol, 2000. **128**: p. 211.
88. Faraday, M., *I. Experimental researches in electricity.—Nineteenth series*. Philosophical Transactions of the Royal Society of London, 1846(136): p. 1-20.
89. Zvezdin, A.K. and V.a.c.A. Kotov, *Modern magneto-optics and magneto-optical materials*. 1997: CRC Press.
90. Hougen, J.T., *Anomalous Faraday Dispersion of O₂*. The Journal of Chemical Physics, 1960. **32**(4): p. 1122-1125.
91. Kerr, J., *XLIII. On rotation of the plane of polarization by reflection from the pole of a magnet*. The London, Edinburgh, and Dublin Philosophical Magazine and Journal of Science, 1877. **3**(19): p. 321-343.

92. Qiu, Z.Q. and S.D. Bader, *Surface magneto-optic Kerr effect*. Review of Scientific Instruments, 2000. **71**(3): p. 1243-1255.
93. Zak, J., et al., *Universal approach to magneto-optics*. Journal of Magnetism and Magnetic Materials, 1990. **89**(1-2): p. 107-123.
94. Yang, Z.J. and M.R. Scheinfein, *Combined three - axis surface magneto - optical Kerr effects in the study of surface and ultrathin - film magnetism*. Journal of Applied Physics, 1993. **74**(11): p. 6810-6823.
95. Mallmann, E., et al. *Yttrium iron garnet: properties and applications review*. in *Solid State Phenomena*. 2013. Trans Tech Publ.
96. Anderson, E.E., *Molecular field model and the magnetization of YIG*. Physical Review, 1964. **134**(6A): p. A1581.
97. Uchida, K.-i., et al., *Quantitative temperature dependence of longitudinal spin Seebeck effect at high temperatures*. Physical Review X, 2014. **4**(4): p. 041023.
98. Khitun, A., *Multi-frequency magnonic logic circuits for parallel data processing*. Journal of Applied Physics, 2012. **111**(5): p. 054307.
99. Glass, H. and M. Elliot, *Attainment of the intrinsic FMR linewidth in yttrium iron garnet films grown by liquid phase epitaxy*. Journal of Crystal Growth, 1976. **34**(2): p. 285-288.
100. Jungfleisch, M.B., et al., *Improvement of the yttrium iron garnet/platinum interface for spin pumping-based applications*. Applied Physics Letters, 2013. **103**(2): p. 022411.
101. Sun, Y., et al., *Damping in Yttrium Iron Garnet Nanoscale Films Capped by Platinum*. Physical Review Letters, 2013. **111**(10).
102. Rezende, S.M., et al., *Enhanced spin pumping damping in yttrium iron garnet/Pt bilayers*. Applied Physics Letters, 2013. **102**(1): p. 012402.
103. Liu, T., et al., *Ferromagnetic resonance of sputtered yttrium iron garnet nanometer films*. Journal of Applied Physics, 2014. **115**(17): p. 17A501.
104. Lustikova, J., et al., *Spin current generation from sputtered Y3Fe5O12 films*. Journal of Applied Physics, 2014. **116**(15): p. 153902.

105. Wang, H.L., et al., *Large spin pumping from epitaxial Y₃Fe₅O₁₂ thin films to Pt and W layers*. Physical Review B, 2013. **88**(10).
106. Bertaut, F. and F. Forrat, *Structure des ferrites ferrimagnétiques des terres rares*. Comptes Rendus Hebdomadaires Des Seances De L Academie Des Sciences, 1956. **242**(3): p. 382-384.
107. Geller, S. and M. Gilleo, *The crystal structure and ferrimagnetism of yttrium-iron garnet, Y₃Fe₂ (FeO₄)₃*. Journal of Physics and Chemistry of solids, 1957. **3**(1-2): p. 30-36.
108. Wettling, W., et al., *Optical absorption and Faraday rotation in yttrium iron garnet*. physica status solidi (b), 1973. **59**(1): p. 63-70.
109. Hunter, I. and J.D. Rhodes, *Electronically tunable microwave bandpass filters*. IEEE Transactions on Microwave Theory and Techniques, 1982. **30**(9): p. 1354-1360.
110. Boudiar, T., et al., *Magneto-optical properties of yttrium iron garnet (YIG) thin films elaborated by radio frequency sputtering*. Journal of magnetism and magnetic materials, 2004. **284**: p. 77-85.
111. Riedel, E., *Moderne anorganische Chemie, Walther de Gruyter GmbH & Co.* 2007, KG.
112. Ibrahim, N., C. Edwards, and S. Palmer, *Pulsed laser ablation deposition of yttrium iron garnet and cerium-substituted YIG films*. Journal of magnetism and magnetic materials, 2000. **220**(2-3): p. 183-194.
113. Du, C., et al., *Y₃Fe₅O₁₂ spin pumping for quantitative understanding of pure spin transport and spin Hall effect in a broad range of materials*. Journal of Applied Physics, 2015. **117**(17): p. 172603.
114. Özgür, Ü., Y. Alivov, and H. Morkoç, *Microwave ferrites, part 2: passive components and electrical tuning*. Journal of Materials Science: Materials in Electronics, 2009. **20**(10): p. 911-952.
115. Henry, R., et al., *Ferromagnetic resonance properties of LPE YIG films*. IEEE Transactions on Magnetics, 1973. **9**(3): p. 535-537.

116. Linares, R.C., R.B. McGraw, and J.B. Schroeder, *Growth and Properties of Yttrium Iron Garnet Single - Crystal Films*. Journal of Applied Physics, 1965. **36**(9): p. 2884-2886.
117. Dorsey, P.C., et al., *Epitaxial yttrium iron garnet films grown by pulsed laser deposition*. Journal of Applied Physics, 1993. **74**(2): p. 1242-1246.
118. Myung-Beom, P., K. Byung Jin, and C. Nam-Hee, *Chemical composition, microstructure and magnetic characteristics of yttrium iron garnet (YIG, Ce:YIG) thin films grown by rf magnetron sputter techniques*. IEEE Transactions on Magnetics, 1999. **35**(5): p. 3049-3051.
119. Krockenberger, Y., et al., *Layer-by-layer growth and magnetic properties of Y₃Fe₅O₁₂ thin films on Gd₃Ga₅O₁₂*. Journal of Applied Physics, 2009. **106**(12): p. 123911.
120. Manuilov, S.A. and A.M. Grishin, *Pulsed laser deposited Y₃Fe₅O₁₂ films: Nature of magnetic anisotropy II*. Journal of Applied Physics, 2010. **108**(1): p. 013902.
121. Yamamoto, S., et al., *Post-annealing effect of YIG ferrite thin-films epitaxially grown by reactive sputtering*. physica status solidi (a), 2004. **201**(8): p. 1810-1814.
122. Sung, S.-Y., X. Qi, and B.J.H. Stadler, *Integrating yttrium iron garnet onto nongarnet substrates with faster deposition rates and high reliability*. Applied Physics Letters, 2005. **87**(12): p. 121111.
123. Kang, Y.-M., et al., *Magnetic properties of YIG (Y₃Fe₅O₁₂) thin films prepared by the post annealing of amorphous films deposited by rf-magnetron sputtering*. Journal of Applied Physics, 2005. **97**(10): p. 10A319.
124. Vossen, J.L., W. Kern, and W. Kern, *Thin film processes II*. Vol. 2. 1991: Gulf Professional Publishing.
125. Lenz, J.E., *A review of magnetic sensors*. Proceedings of the IEEE, 1990. **78**(6): p. 973-989.
126. Coey, J.M., *Magnetism and magnetic materials*. 2010: Cambridge university press.
127. London, F., *Superfluids New York*. 1950, Wiley.

128. Josephson, B.D., *Possible new effects in superconductive tunnelling*. Physics letters, 1962. **1**(7): p. 251-253.
129. Josephson, B.D., *The discovery of tunnelling supercurrents*. Reviews of Modern Physics, 1974. **46**(2): p. 251.
130. Gurevich, A.G. and G.A. Melkov, *Magnetization oscillations and waves*. 2020: CRC press.
131. Urban, R., G. Woltersdorf, and B. Heinrich, *Gilbert Damping in Single and Multilayer Ultrathin Films: Role of Interfaces in Nonlocal Spin Dynamics*. Physical Review Letters, 2001. **87**(21).
132. Oogane, M., et al., *Magnetic Damping in Ferromagnetic Thin Films*. Japanese Journal of Applied Physics, 2006. **45**(5A): p. 3889-3891.
133. Zhang, Z., et al., *Angular dependence of ferromagnetic resonance in exchange-coupled Co/Ru/Co trilayer structures*. Physical Review B, 1994. **50**(9): p. 6094-6112.
134. Heinrich, B., et al., *Dynamic Exchange Coupling in Magnetic Bilayers*. Physical Review Letters, 2003. **90**(18).
135. Nascimento, V.P., et al., *Ferromagnetic resonance study of the exchange bias field in NiFe / FeMn / NiFe trilayers*. Journal of Applied Physics, 2006. **99**(8): p. 08C108.
136. Chikazumi, S. and C.D. Graham, *Physics of ferromagnetism*. 1997: Oxford university press.
137. Kalarickal, S.S., et al., *Ferromagnetic resonance linewidth in metallic thin films: Comparison of measurement methods*. Journal of Applied Physics, 2006. **99**(9): p. 093909.
138. Nembach, H.T., et al., *Perpendicular ferromagnetic resonance measurements of damping and Landé-factor in sputtered (Co₂Mn)_{1-x}Gex thin films*. Physical Review B, 2011. **84**(5).
139. Shaw, J.M., H.T. Nembach, and T.J. Silva, *Determination of spin pumping as a source of linewidth in sputtered Co₉₀Fe₁₀/Pd multilayers by use of broadband ferromagnetic resonance spectroscopy*. Physical Review B, 2012. **85**(5).

140. Nembach, H., et al., *Perpendicular ferromagnetic resonance measurements of damping and Landé g-factor in sputtered (Co₂Mn)_{1-x}Ge_x thin films*. Physical review B, 2011. **84**(5): p. 054424.
141. Shaw, J.M., H.T. Nembach, and T.J. Silva, *Damping phenomena in Co₉₀Fe₁₀/Ni multilayers and alloys*. Applied Physics Letters, 2011. **99**(1): p. 012503.
142. Bilzer, C., et al., *Vector network analyzer ferromagnetic resonance of thin films on coplanar waveguides: Comparison of different evaluation methods*. Journal of applied physics, 2007. **101**(7): p. 074505.
143. Wang, K.F., J.M. Liu, and Z.F. Ren, *Multiferroicity: the coupling between magnetic and polarization orders*. Advances in Physics, 2009. **58**(4): p. 321-448.
144. Ramesh, R. and N.A. Spaldin, *Multiferroics: progress and prospects in thin films*. Nature materials, 2007. **6**(1): p. 21-29.
145. Cheong, S.-W. and M. Mostovoy, *Multiferroics: a magnetic twist for ferroelectricity*. Nature Materials, 2007. **6**(1): p. 13-20.
146. Hur, N., et al., *Electric polarization reversal and memory in a multiferroic material induced by magnetic fields*. Nature, 2004. **429**(6990): p. 392-395.
147. Curie, P., *Sur la symétrie dans les phénomènes physiques, symétrie d'un champ électrique et d'un champ magnétique*. Journal de physique théorique et appliquée, 1894. **3**(1): p. 393-415.
148. Astov, D., *The magnetoelectric effect in antiferromagnets*. Sov. Phys. JETP, 1960. **11**: p. 708.
149. Rado, G.T. and V.J. Folen, *Observation of the Magnetically Induced Magnetoelectric Effect and Evidence for Antiferromagnetic Domains*. Physical Review Letters, 1961. **7**(8): p. 310-311.
150. Folen, V.J., G.T. Rado, and E.W. Stalder, *Anisotropy of the Magnetoelectric Effect in Cr₂O₃*. Physical Review Letters, 1961. **6**(11): p. 607-608.
151. Wang, J., et al., *Epitaxial BiFeO₃ multiferroic thin film heterostructures*. science, 2003. **299**(5613): p. 1719-1722.

152. Zheng, H., et al., *Multiferroic batio₃-cofe₂o₄ nanostructures*. Science, 2004. **303**(5658): p. 661-663.
153. Wood, V.E. and A. AE, *Possible applications for magnetoelectric materials*. 1974.
154. Diao, Z., et al., *Spin transfer switching and spin polarization in magnetic tunnel junctions with MgO and AlOx barriers*. Applied Physics Letters, 2005. **87**(23): p. 232502.
155. Sahoo, S., et al., *Ferroelectric control of magnetism in Ba Ti O 3 / Fe heterostructures via interface strain coupling*. Physical Review B, 2007. **76**(9): p. 092108.
156. Spaldin, N.A. and R. Ramesh, *Electric-field control of magnetism in complex oxide thin films*. MRS bulletin, 2008. **33**(11): p. 1047-1050.
157. Baek, S., et al., *Ferroelastic switching for nanoscale non-volatile magnetoelectric devices*. Nature materials, 2010. **9**(4): p. 309-314.
158. Chu, Y.-H., et al., *Electric-field control of local ferromagnetism using a magnetoelectric multiferroic*. Nature materials, 2008. **7**(6): p. 478-482.
159. King-Smith, R.D. and D. Vanderbilt, *Theory of polarization of crystalline solids*. Physical Review B, 1993. **47**(3): p. 1651-1654.
160. Resta, R., *Macroscopic polarization in crystalline dielectrics: the geometric phase approach*. Reviews of Modern Physics, 1994. **66**(3): p. 899-915.
161. Schmid, H., *Multi-ferroic magnetoelectrics*. Ferroelectrics, 1994. **162**(1): p. 317-338.
162. Kimura, T., et al., *Magnetic control of ferroelectric polarization*. Nature, 2003. **426**(6962): p. 55-58.
163. Lottermoser, T., et al., *Magnetic phase control by an electric field*. Nature, 2004. **430**(6999): p. 541-544.
164. Dong, S., et al., *Multiferroic materials and magnetoelectric physics: symmetry, entanglement, excitation, and topology*. Advances in Physics, 2015. **64**(5-6): p. 519-626.

165. Tabuchi, Y., et al., *Coherent coupling between a ferromagnetic magnon and a superconducting qubit*. Science, 2015. **349**(6246): p. 405-408.
166. McKenzie-Sell, L., et al., *Low-impedance superconducting microwave resonators for strong coupling to small magnetic mode volumes*. Physical Review B, 2019. **99**(14).
167. Li, Y., et al., *Strong Coupling between Magnons and Microwave Photons in On-Chip Ferromagnet-Superconductor Thin-Film Devices*. Physical Review Letters, 2019. **123**(10).
168. Hou, J.T. and L. Liu, *Strong coupling between microwave photons and nanomagnet magnons*. Physical Review Letters, 2019. **123**(10): p. 107702.
169. Huebl, H., et al., *High Cooperativity in Coupled Microwave Resonator Ferrimagnetic Insulator Hybrids*. Physical Review Letters, 2013. **111**(12).
170. Zhang, X., et al., *Strongly Coupled Magnons and Cavity Microwave Photons*. Physical Review Letters, 2014. **113**(15).
171. Miroshnichenko, A.E., et al., *Nonlinear Fano resonance and bistable wave transmission*. Physical Review E, 2005. **71**(3).
172. Limonov, M.F., et al., *Fano resonances in photonics*. Nature Photonics, 2017. **11**(9): p. 543-554.
173. Peng, B., et al., *What is and what is not electromagnetically induced transparency in whispering-gallery microcavities*. Nature Communications, 2014. **5**(1): p. 5082.
174. Weis, S., et al., *Optomechanically induced transparency*. Science, 2010. **330**(6010): p. 1520-1523.
175. Safavi-Naeini, A.H., et al., *Electromagnetically induced transparency and slow light with optomechanics*. Nature, 2011. **472**(7341): p. 69-73.
176. Xiong, Y., et al., *Probing magnon–magnon coupling in exchange coupled $Y_3Fe_5O_{12}$ /Permalloy bilayers with magneto-optical effects*. Scientific Reports, 2020. **10**(1).
177. Yoon, S., J. Liu, and R.D. McMichael, *Phase-resolved ferromagnetic resonance using a heterodyne detection method*. Physical Review B, 2016. **93**(14).

178. Li, Y., et al., *Simultaneous Optical and Electrical Spin-Torque Magnetometry with Phase-Sensitive Detection of Spin Precession*. Physical Review Applied, 2019. **11**(3).
179. Klingler, S., et al., *Spin-Torque Excitation of Perpendicular Standing Spin Waves in Coupled YIG/Co Heterostructures*. Physical Review Letters, 2018. **120**(12).
180. Chen, J., et al., *Strong Interlayer Magnon-Magnon Coupling in Magnetic Metal-Insulator Hybrid Nanostructures*. Physical Review Letters, 2018. **120**(21).
181. Qin, H., S.J. Hämäläinen, and S. Van Dijken, *Exchange-torque-induced excitation of perpendicular standing spin waves in nanometer-thick YIG films*. Scientific Reports, 2018. **8**(1).
182. Li, Y., et al., *Coherent Spin Pumping in a Strongly Coupled Magnon-Magnon Hybrid System*. Physical Review Letters, 2020. **124**(11).
183. Liensberger, L., et al., *Spin-Wave Propagation in Metallic $\text{Co}_{25}\text{Fe}_{75}$ Films Determined by Microfocused Frequency-Resolved Magneto-Optic Kerr Effect*. IEEE Magnetics Letters, 2019. **10**: p. 1-5.
184. Peng, B., et al., *What is and what is not electromagnetically induced transparency in whispering-gallery microcavities*. Nature communications, 2014. **5**(1): p. 1-9.
185. Safavi-Naeini, A.H., et al., *Electromagnetically induced transparency and slow light with optomechanics*. Nature, 2011. **472**(7341): p. 69-73.
186. Khomskii, D., *Classifying multiferroics: Mechanisms and effects*. Physics, 2009. **2**: p. 20.
187. Kimura, T., *Magnetoelectric Hexaferrites*. Annual Review of Condensed Matter Physics, 2012. **3**(1): p. 93-110.
188. Fusil, S., et al., *Magnetoelectric Devices for Spintronics*. Annual Review of Materials Research, 2014. **44**(1): p. 91-116.
189. Sundaresan, N.M., et al., *Beyond strong coupling in a multimode cavity*. Physical Review X, 2015. **5**(2): p. 021035.
190. Moores, B.A., et al., *Cavity quantum acoustic device in the multimode strong coupling regime*. Physical review letters, 2018. **120**(22): p. 227701.

191. Kostylev, N., M. Goryachev, and M.E. Tobar, *Superstrong coupling of a microwave cavity to yttrium iron garnet magnons*. Applied Physics Letters, 2016. **108**(6): p. 062402.
192. Zhang, W., et al., *Spin pumping and inverse spin Hall effects—Insights for future spin-orbitronics*. Journal of Applied Physics, 2015. **117**(17): p. 172610.
193. Ramaswamy, R., et al., *Recent advances in spin-orbit torques: Moving towards device applications*. Applied Physics Reviews, 2018. **5**(3): p. 031107.
194. Baltz, V., et al., *Antiferromagnetic spintronics*. Reviews of Modern Physics, 2018. **90**(1): p. 015005.
195. Zhang, W. and K.M. Krishnan, *Epitaxial exchange-bias systems: From fundamentals to future spin-orbitronics*. Materials Science and Engineering: R: Reports, 2016. **105**: p. 1-20.
196. Liensberger, L., et al., *Exchange-enhanced ultrastrong magnon-magnon coupling in a compensated ferrimagnet*. Physical review letters, 2019. **123**(11): p. 117204.
197. MacNeill, D., et al., *Control of spin-orbit torques through crystal symmetry in WTe₂/ferromagnet bilayers*. Nature Physics, 2017. **13**(3): p. 300-305.
198. Zhang, W., et al., *Research Update: Spin transfer torques in permalloy on monolayer MoS₂*. APL Materials, 2016. **4**(3): p. 032302.
199. Li, Y., et al., *Gate-tuned temperature in a hexagonal boron nitride-encapsulated 2-D semiconductor device*. IEEE Transactions on Electron Devices, 2018. **65**(10): p. 4068-4072.
200. Zhang, X., *Characterization of layer number of two-dimensional transition metal diselenide semiconducting devices using Si-peak analysis*. Advances in Materials Science and Engineering, 2019. **2019**.
201. Mellnik, A., et al., *Spin-transfer torque generated by a topological insulator*. Nature, 2014. **511**(7510): p. 449-451.
202. Li, P., et al., *Magnetization switching using topological surface states*. Science advances, 2019. **5**(8): p. eaaw3415.